Mathematical Modeling and Experimental Investigations of the Charge–Discharge Mechanisms in Aqueous Batteries

Sidian Chen,[†,§] Sofia K. Catalina,[‡,§] William C. Chueh,[*,‡,¶,†] and Hamdi A. Tchelepi[*,†]

[†]*Department of Energy Science & Engineering, Stanford University, United States.*

[‡]*Department of Materials Science & Engineering, Stanford University, United States*

[¶]*Stanford Institute for Materials and Energy Sciences, SLAC National Accelerator Laboratory, Menlo Park, CA, USA.*

[§]*These authors contributed equally to this work.*

E-mail: wchueh@stanford.edu; tchelepi@stanford.edu

Abstract

Rechargeable aqueous batteries are ideal candidates for grid-scale energy storage due to their inherent safety and the abundance and low cost of their electrochemically active materials. However, realizing high-capacity and low-cost aqueous batteries is limited by significant coulombic and voltaic inefficiencies during charge–discharge cycles. To examine the underlying mechanisms of these inefficiencies, we develop a one-dimensional continuum-scale model to simulate the reactive and charge transport processes in aqueous batteries and assess their impacts on the charge–discharge performance. The model accounts for multiple chemical and electrochemical reactions (e.g., nucleation, deposition, dissolution, gas evolution, and intercalation) and

reaction-induced variations in electrolyte pH and reactive surface areas. We fit the model to experimentally-measured charge–discharge curves for several aqueous battery chemistries, including acidic H_2–Mn, near-neutral Zn–MnO_2, and alkaline Sn–NiOOH chemistries. We also incorporate additional physics into the model to simulate more complex phenomena such as nucleation overpotential and adsorption energy. The modeling framework provides a mechanistic tool for studying the physical, chemical, and electrochemical processes in aqueous batteries; and guides the design of high-utilization and low-cost aqueous batteries for grid-scale energy storage.

1 Introduction

Rechargeable aqueous batteries utilize water as the electrolyte solvent and abundant low-toxicity metal elements as the primary reactants. While the inherent safety and affordability of their active materials make them strong candidates for grid-scale energy storage, their commercial viability hinges on achieving higher energy densities. One of the most promising strategies is to construct electrodes using multi-electron metal deposition/stripping reactions, such as two- (Mn, Zn, Ca, Mg), three- (Fe, Al), and four- (Sn) electron metal reactions. For example, the theoretical energy densities of acidic MnO_2, near-neutral Zn, and alkaline Sn electrodes (respectively 617, 820, and 903 mAh/g), which though lower than that of lithium metal (3860 mAh/g) are substantially higher than that of conventional lithium-ion intercalation electrodes (e.g., graphite at 372 mAh/g). While several aqueous battery systems using multi-electron metal electrodes have been demonstrated[1–5], most studies operate under low utilization conditions where only a small fraction of the electrochemically active material participates in the electrochemical reactions and energy conversion. Consequently, the realized cell capacities often fall short of theoretical limits, and the total lifetime energy throughput is limited (Figure 1). Achieving high energy density and long cycle life remains challenging, primarily due to significant coulombic and voltaic inefficiencies at higher utilization levels.

Coulombic and voltaic inefficiencies in aqueous batteries stem from various mechanisms.

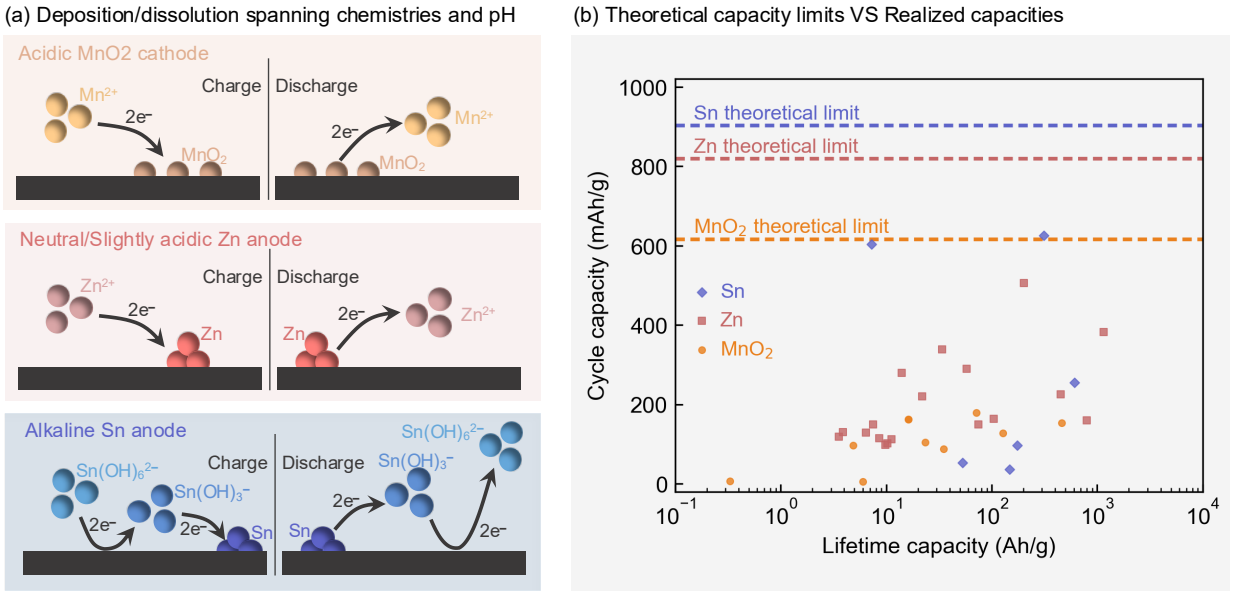

Figure 1: (a) Electrochemical deposition and dissolution reactions in aqueous batteries using acidic MnO_2 cathode, near-neutral Zn anode, and alkaline Sn anode. (b) Theoretical capacity limits, realized cycle capacities, and realized lifetime capacities of the three electrode types. The realized cycle capacities and life-time capacities were collected from the literature, where cell capacities and electrode-deposited active material mass are provided. The data and references are presented in Table S1.

First, electro-deposition and electro-dissolution reactions—common processes in aqueous battery electrodes wherein the active material undergoes a redox transformation between liquid and solid phases—may consume additional energy through processes like nucleation and surface adsorption, generate high-resistance solids, or even form irreversible oxides[6,7]. Second, when electrode potentials fall outside the water stability window, gas evolution such as the hydrogen evolution reaction (HER) and oxygen evolution reaction (OER) may occur[8]. In particular, HER occurs at reductive potentials and becomes more active in acidic electrolytes where the hydrogen evolution activity of metals (e.g., Al) increases. The gas generation process, if irreversible, can result in capacity loss through a variety of mechanisms, including blockage of electrode reactive sites[9], consumption of water[10], and precipitation of electroactive salts. Finally, the chemical reactivity of electroactive ions and deposited metals can cause self-discharge reactions that significantly reduce cell capacity and energy efficiency[4]. Addressing these challenges requires mechanistic investigations on the transport,

chemical, and electrochemical processes in aqueous batteries during cycling.

Physics-based models provide mechanistic tools to characterize the intertwined transport and reaction processes in battery cells as demonstrated by the pioneering work of Newman and Tobias[11] on general porous electrodes, as well as more recent studies on other battery systems (e.g., lithium-ion battery[12,13], lithium–sulfur battery[14–16], and zinc–air battery[17]). Despite the progress in Li- and zinc–air battery systems, physics-based models for rechargeable aqueous batteries remain limited[18,19]. The challenge arises from the different and often elusive reaction mechanisms in aqueous batteries. For example, electrochemical and chemical reactions can significantly alter the electrolyte pH spatially and temporally through conversion, production, or consumption of protons (H^+) and hydroxides (OH^-)[20–22]. Fluctuations in pH, in conjunction with electrode potential govern ion speciation, reaction pathways, and reaction kinetics in aqueous electrolytes[19,23]. Additionally, aqueous battery electrodes often undergo electrochemical deposition/dissolution reactions and chemical precipitation/dissolution reactions[3,20,24], which modify the electrode surface morphology and reactive surface area. The reactive surface area is critical to the charge–discharge performance as it controls the rates of electro-deposition and electro-dissolution reactions. Accurate representations of electrolyte pH and reactive surface area are essential for predicting charge–discharge behaviors and resolving the underlying physical, chemical, and electrochemical reactions.

To our knowledge, two physics-based aqueous battery models have been reported in the literature[18,19]. Bernard et al.[18] introduced a one-dimensional continuum-scale model to simulate the discharge curves of an MnO_2 cathode for near-neutral aqueous Zn–MnO_2 batteries. Their model did not account for local or bulk pH change, nor its effect on reaction kinetics and discharge behavior (e.g., the pH-driven precipitation of zinc hydroxide sulfate (ZHS)). While they recently extended the model to account for pH variations[25], it remains unclear how changes in porosity and reactive surface area were represented in their model. Concurrently, Herrmann et al.[19] extended a pseudo-two-dimensional (P2D) continuum-scale model

for a Zn–air battery model[17] to study the interplay between electrolyte pH and reactions at the MnO_2 cathode of aqueous Zn–MnO_2 batteries. Their model estimated the reactive surface areas by representing the cathode active materials as non-overlapping spherical particles. It does not account for the generation of new reactive surfaces induced by particle separations during dissolution, as well as the coalescence of particle reactive surfaces during deposition. To date, these models have focused exclusively on aqueous Zn–MnO_2 batteries. Consequently, it remains unclear whether they can be generalized and applied to other aqueous battery chemistries with different pH and reaction pathways.

To bridge these gaps, we develop a one-dimensional continuum-scale model for aqueous battery cells that expands on previous aqueous battery models and can be used to examine various chemistries and pHs. Our model represents a full aqueous battery cell as a one-dimensional continuum accounting for multispecies ion and charge transport, chemical and electrochemical reactions (e.g., nucleation, deposition, dissolution, gas evolution, and intercalation), and reaction-induced variations in electrolyte pH and reactive solid surface areas in the liquid electrolyte, solid matrix, or their interfaces. We apply the model to study various aqueous battery chemistries (including acidic H_2-Mn, near-neutral Zn-MnO_2, and alkaline Sn-NiOOH) and their cycling performance across diverse initial, boundary, and operating conditions. Our comprehensive model–experimental data comparisons and validations demonstrate the capability of the modeling framework to deepen the mechanistic understanding of electrode processes and provide necessary insights to improve battery performance.

2 Methods

We summarize the reaction mechanisms in the studied aqueous batteries (Section 2.1). We then formulate a general mathematical model for aqueous battery cells (Section 2.2) and present the numerical algorithm for solving the model (Section 2.3). Finally, we benchmark

the model using experimental data (Section 2.4).

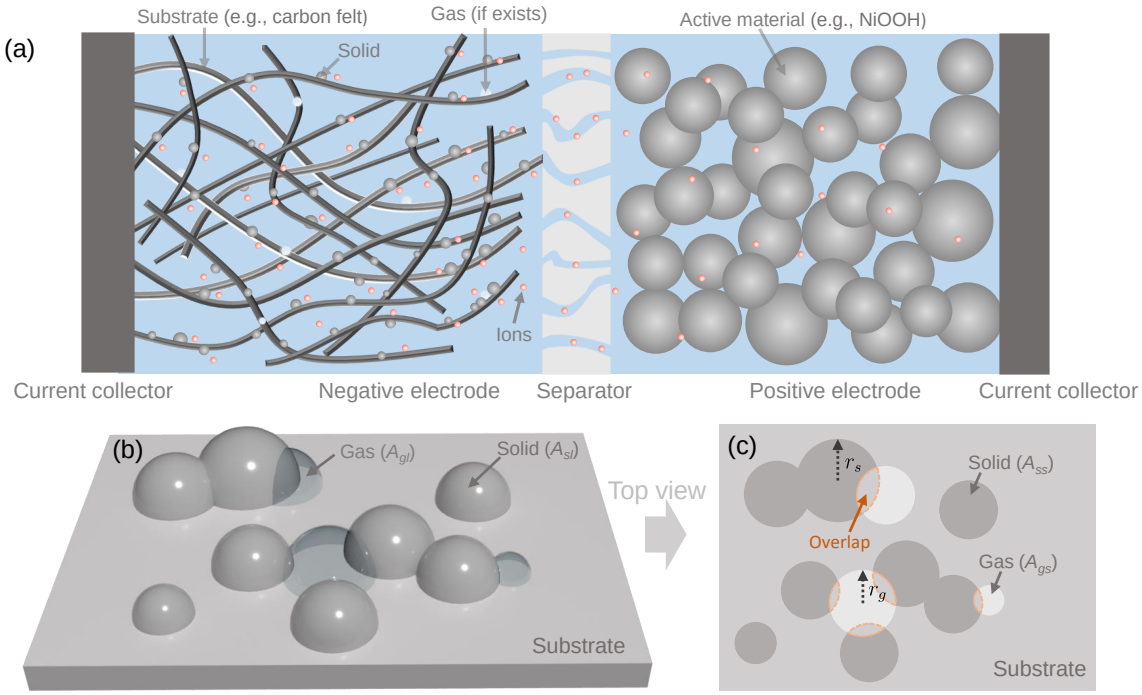

Figure 2: (a) An example aqueous battery (i.e., aqueous alkaline Sn-NiOOH battery) consisting of a negative electrode substrate with electro-deposited materials, a separator, and a positive electrode. (b) Three-dimensional representations and (c) top planar view of the electro-deposited solids and generated gases represented by fully penetrable hemispheres. The electrodeposition is represented as a single layer of solid spheres, which will coalesce into a dense solid. The gas generation is represented by a single layer of gas spheres, which will coalesce into a large gas bubble alongside or on top of the dense solid.

2.1 Reaction mechanisms

2.1.1 Acidic H_2–Mn battery

Acidic H_2–Mn aqueous batteries utilize reversible HER as the anode reaction and MnO_2 deposition/dissolution as the cathode reaction. The electrochemical and chemical reactions in the acidic H_2-Mn battery anode (Equations (1–2)) and cathode (Equation (3)) are[20]:

$$H_2(g) \leftrightarrow H_2(aq), \tag{1}$$

$$\mathrm{H_2(aq)} \leftrightarrow 2\mathrm{H^+} + 2\mathrm{e^-}, \tag{2}$$

$$\mathrm{MnO_2(s)} + 4\mathrm{H^+} + 2\mathrm{e^-} \leftrightarrow \mathrm{Mn^{2+}} + 2\mathrm{H_2O(l)}, \tag{3}$$

where "g", "s", "l", and "aq" denote gas, solid, liquid, and dissolved gas phases.

2.1.2 Near-neutral Zn–MnO_2 battery

In near-neutral Zn–MnO_2 batteries, the electro-deposition and electro-dissolution of Zn are the only electrochemical reactions in the Zn anode. However, it remains under debate which electrochemical reactions occur in the MnO_2 cathode. Existing hypotheses include: (1) Zn^{2+} (de)intercalation[26], (2) H^+ (de)intercalation (or conversion reaction)[24], (3) zinc hydroxide sulfate (ZHS) deposition/dissolution[22], (4) Zn–Mn compound deposition/dissolution[21], (5) MnOOH disproportionation[27], and others. Based on existing experimental observations[22,24,26] and theoretical analysis[28], reaction pathways (1)–(3) appear plausible and are thus used to parameterize the model. The electrochemical and chemical reactions in the anode (Equation (4)) and the cathode (Equations (5–7)) are:

$$\mathrm{Zn(s)} \leftrightarrow \mathrm{Zn^{2+}} + 2\mathrm{e^-}, \tag{4}$$

$$2\mathrm{MnO_2(s)} + \mathrm{Zn^{2+}} + 2\mathrm{e^-} \leftrightarrow \mathrm{ZnMn_2O_4(s)}, \tag{5}$$

$$\mathrm{MnO_2(s)} + \mathrm{H^+} + \mathrm{e^-} \leftrightarrow \mathrm{MnOOH(s)}, \tag{6}$$

$$4\mathrm{Zn^{2+}} + \mathrm{SO_4^{2-}} + 6\mathrm{OH^-} + x\mathrm{H_2O} \leftrightarrow \mathrm{Zn_4SO_4(OH)_6} \cdot x\mathrm{H_2O(s)}. \tag{7}$$

2.1.3 Alkaline Sn–NiOOH battery

Alkaline Sn–NiOOH batteries take advantage of the four-electron reaction between Sn and $Sn(OH)_6^{2-}$ in the anode and H^+ (de)intercalation in NiOOH in the cathode.[4] During the charge and discharge of alkaline Sn–NiOOH batteries, the desired anode (Equations (8–

9)) and cathode (Equation (11)) reactions are complicated by the chemical reactivity of the $Sn(OH)_3^-$ intermediate, which can chemically disproportionate (Equation (10)) or chemically react with the cathode in a self-discharge mechanism (Equation (12)). The electrochemical and chemical reactions involved are summarized below.

$$Sn(s) + 3OH^- \leftrightarrow Sn(OH)_3^- + 2e^-, \tag{8}$$

$$Sn(OH)_3^- + 3OH^- \leftrightarrow Sn(OH)_6^{2-} + 2e^-, \tag{9}$$

$$2Sn(OH)_3^- \leftrightarrow Sn(s) + Sn(OH)_6^{2-}, \tag{10}$$

$$NiOOH(s) + H_2O(l) + e^- \leftrightarrow Ni(OH)_2(s) + OH^-, \tag{11}$$

$$2NiOOH(s) + Sn(OH)_3^- + OH^- + 2H_2O(l) \leftrightarrow 2Ni(OH)_2(s) + Sn(OH)_6^{2-}. \tag{12}$$

2.2 Mathematical model

2.2.1 Electrochemical and chemical reactions

We consider a full aqueous battery cell (Figure 2a), structured as a layered assembly of three solid domains—the negative electrode, separator, and positive electrode—immersed in a liquid electrolyte. During the charge and discharge of the battery cell, the chemical species can participate in electrochemical and chemical reactions (see examples in Section 2.1). To ensure generalizability, we describe each reaction by the following equation:

$$\sum_k s_{jk} M_k^{z_k} = n_k e^-, \tag{13}$$

where j denotes the index of the j^{th} reaction, k denotes the index of k^{th} chemical species, M_k refers to the k^{th} chemical species, z_k is the charge number of M_k, n_j is the number of electrons transferred in the j^{th} reaction ($n_j = 0$ if the j^{th} reaction is a chemical reaction), s_{jk} is the stoichiometric coefficient of the k^{th} chemical species in the j^{th} reaction.

Electrochemical reaction We assume the electrochemical reactions occur at the electrolyte–substrate interface (e.g., electro-deposition and electro-dissolution) or inside the substrate (e.g., intercalation and deintercalation). Supposing the j^{th} reaction is electrochemical, the reaction rate for k^{th} species in the the j^{th} reaction is given by

$$S_{jk} = -A_j \frac{s_{jk} I_j}{n_j F}, \tag{14}$$

where s_{jk} and n_j are defined in Equation (13), F is the Faraday constant, A_j is the specific reactive surface area for the j^{th} reaction (A_j is an important parameter that will be discussed in more details later), and i_j is the current density due to the j^{th} electrochemical reaction. Here, i_j is assumed to follow the Butler–Volmer equation

$$i_j = i_{0,j} \left[\prod_k \left(a_k \frac{c_k}{1000} \right)^{p_{jk}} \exp\left(\frac{\alpha_{aj} F}{R_g T} \eta_j \right) - \prod_k \left(a_k \frac{c_k}{1000} \right)^{q_{jk}} \exp\left(-\frac{\alpha_{cj} F}{R_g T} \eta_j \right) \right], \tag{15}$$

where $i_{0,j}$ is the exchange current density of the j^{th} electrochemical reaction at reference concentrations, a_k is the activity coefficient of the k^{th} species, c_k is the aqueous concentration of the k^{th} species with a unit of mol/m^3, $p_{jk} = \max(s_{jk}, 0)$, $q_{jk} = -\min(s_{jk}, 0)$, α_{aj} and α_{cj} are respectively the anode and cathode transfer coefficient of the j^{th} reaction, η_j is the overpotential for the j^{th} electrochemical reaction. η_j is defined as $\eta_j = \phi_s - \phi_l - U_{eq,j}$, where ϕ_s is the electric potential in the solid substrate, ϕ_l is the electric potential in the liquid electrolyte, and $U_{eq,j}$ is the equilibrium potential for the j^{th} reaction as computed by the Nernst equation.

The reaction rate S_{jk} scales with the reactive surface area A_j, which can be modified by deposition/dissolution reactions and gas generation/consumption reactions. A_j is a function of the interfacial areas between the depositing/dissolving solids, gases, liquid electrolyte, and solid substrate. To differentiate the depositing/dissolving solids from the solid substrate, we will refer to the former as "solid" and the latter as "substrate" hereafter. Assuming only one solid and one gas are generated or consumed by reactions, we represent each phase as

separate, fully penetrable hemispheres, i.e., a single layer of solid spheres which will coalesce into a dense solid and a single layer of gas spheres which will coalesce into a large gas bubble on top of the dense solid (Figure 2b–2c). Accordingly, we can compute their surface areas by a stochastic geometry method, namely a Boolean model[29,30]. According to the Boolean model, the solid–electrolyte interfacial area A_{sl} in a unit control volume is given by

$$A_{sl} = A_{sl}^{e} \exp\left(-\lambda_s \frac{\epsilon_s^e}{\epsilon_0}\right), \tag{16}$$

where A_{sl}^{e} is the extended area of the solid–electrolyte interfaces per unit control volume (defined as $A_{sl}^{e} = \sum_k N_{s,k} 2\pi r_{s,k}^2$, where k refers to the rank of a radius r_s and $N_{s,k}$ is the number of solid-phase hemispheres whose radii are equal to $r_{s,k}$ in a unit control volume), ϵ_s^e is the extended volume fraction of the solid-phase hemispheres (defined as $\epsilon_s^e = \sum_k N_{s,k}(2\pi/3) r_{s,k}^3$), ϵ_0 is the initial substrate porosity without electro-deposition and gas generation, and λ_s is a scale for accounting for the deviation of surface area for non-spherical solids (we set $\lambda_s = 1$ by default, unless stated otherwise). Additionally, we can compute the solid–substrate interfacial area A_{ss} using a two-dimensional version of the Boolean model

$$A_{ss} = A_0 \left[1 - \exp\left(-\lambda_{ss} \frac{A_{ss}^{e}}{A_0}\right)\right], \tag{17}$$

where A_0 is the initial reactive surface area per unit control volume before the occurrence of electro-deposition and gas generation, A_{ss}^{e} is the area of the extended solid-substrate interface per unit control volume (i.e., $A_{ss}^{e} = \sum_k N_{s,k} \pi r_{s,k}^2$), and λ_{ss} is a scale for accounting for the deviation of the solid-substrate interfacial area for non-spherical solids (we set $\lambda_{ss} = 1$ by default, unless stated otherwise).

We apply the same approach to compute the gas-phase surface area and the gas–substrate interfacial area. If no electro-deposition occurs, these areas can be computed using the same equations for the solid phase. If gas evolution is occurring alongside deposition, we need to consider the impact of the solid phase. In that case, we assume the solid phase as the

primary phase and the gas phase as the secondary phase, which will reside in the pore spaces not occupied by the solid phase. Therefore, the gas-phase surface area A_{gl} is given by[29,30]

$$A_{gl} = A^e_{gl} \exp\left(-\lambda_s \frac{\epsilon^e_s}{\epsilon_0}\right) \exp\left(-\lambda_g \frac{\epsilon^e_g}{\epsilon_0}\right), \tag{18}$$

where A^e_{gl} is the extended surface area of the gas phase per unit control volume (defined as $A^e_{gl} = \sum_k N_{g,k} 2\pi r^2_{g,k}$, where $N_{g,k}$ is the number of gas-phase hemispheres whose radii are $r_{g,k}$ in a unit control volume), ϵ^e_g is the extended volume fraction of the gas-phase hemispheres per unit control volume (defined as $\epsilon^e_g = \sum_k N_{g,k}(2\pi/3) r^3_{g,k}$), and λ_g is a scale for accounting for the deviation of the surface area for non-spherical gases (we set $\lambda_g = 1$ by default, unless stated otherwise). Similarly, the gas–substrate interfacial area A_{gs} is given by a two-dimensional version of the Boolean model

$$A_{gs} = A_0 \exp\left(-\lambda_{ss} \frac{A^e_{ss}}{A_0}\right) \left[1 - \exp\left(-\lambda_{gs} \frac{A^e_{gs}}{A_0}\right)\right], \tag{19}$$

where A^e_{gs} is the extended area of the gas–substrate interface per unit control volume (i.e., $A^e_{gs} = \sum_k N_{g,k} \pi r^2_{g,k}$), and λ_{gs} is a scale for accounting for the deviation of gas–substrate interfacial area for non-spherical solids (we set $\lambda_{gs} = 1$ by default, unless stated otherwise).

Additionally, some electro-deposition reactions are typically initiated by a nucleation process where a high overpotential is required to overcome the surface energy barrier and create new solid phases. We model the nucleation using classical nucleation theory and compute the nucleation rate N_{jk} (i.e., the number of newly formed nuclei in a unit control volume) for the j^{th} reaction by

$$\frac{\mathrm{d}N_{jk}}{\mathrm{d}t} = A_{ns,j} Z_{jk} f_{jk} \exp\left(-\frac{\Delta G_{jk}}{k_b T}\right), \tag{20}$$

where $A_{ns,j}$ is the specific area of nucleation sites (we assume $A_{ns,j} = \max(A_0 - A_{ss} - A_{gs}, 0)$), Z_{jk} is the probability of forming a stable nucleus of the k^{th} species per unit surface area, f_{jk}

is the frequency at which an atom or molecule of the k^{th} species to attaches to the nucleus, k_b is the Boltzmann constant, and ΔG_{jk} is the net change in Gibbs free energy upon forming a nucleus, which is a function of nucleus radius $r_{n,jk}$. ΔG_{jk}, which changes over time, is given by

$$\Delta G_{jk} = \frac{2}{3}\pi r_{n,jk}^3 \frac{\rho_{s,jk} n_j F}{s_{jk}}(\phi_s - \phi_l) + \pi r_{n,jk}^2(\gamma_{ns,jk} - \gamma_{ls,jk}) + 2\pi r_{n,jk}^2 \gamma_{ln,jk}, \tag{21}$$

where $\rho_{s,jk}$ is the molar density of the solid phase; $\gamma_{ns,jk}$, $\gamma_{ls,jk}$, and $\gamma_{ln,jk}$ are the interfacial tensions between the nucleus and substrate, the liquid electrolyte and substrate, and the liquid electrolyte and nucleus, respectively. Following classical nucleation theory, we assume a stable nucleus will only form if its radius is greater than a critical size r^c given by

$$r_{n,jk}^c = -\frac{s_{jk}\left(\gamma_{ns,jk} - \gamma_{ls,jk} + 2\gamma_{ln,jk}\right)}{\rho_{s,jk} n_j F(\phi_s - \phi_l)}. \tag{22}$$

In the presence of nucleation, the reaction rate for the k^{th} species in the j^{th} electrochemical reaction becomes

$$S_{jk} = -A_j \frac{s_{jk} i_j}{n_j F} = -(A_{n,j} + A_{d,j}) \frac{s_{jk} i_j}{n_j F}, \tag{23}$$

where $A_{n,j}$ is the surface area of all nuclei in a unit control volume (i.e., $A_{n,j}$ can be computed by $A_{n,j} = A_{sl}^e \left[1 - \exp\left(-\epsilon_n^e/\epsilon_0\right)\right]\left[1 - \exp\left(-\epsilon_s^e/\epsilon_0\right)\right]$, where ϵ_n^e is the extended volume fraction of the nuclei) and $A_{d,j}$ is the depositing solid-phase surface area (i.e., $A_{d,j} = A_{sl}^e \exp\left(-\epsilon_n^e/\epsilon_0\right)\left[1 - \exp\left(-\epsilon_s^e/\epsilon_0\right)\right]$).

As discussed earlier in this section, the reactive surface area for the j^{th} reaction A_j is a function of A_{sl}, A_{ss}, A_{gl}, A_{gs}, and A_0. The exact expressions of the functions depend on the specific reactions and the solid-phase electrical conductivity, which are specified in Table S6 for several aqueous batteries.

Chemical reactions Chemical reactions may occur in the electrolyte, on the substrate surface, or on the solid surface. Supposing the j^{th} reaction is a chemical reaction, the reaction

rate for k^{th} species in the the j^{th} reaction is given by

$$S_{jk} = -\beta_j s_{jk} \left[K_{f,j} \prod_k \left(a_k \frac{c_k}{1000} \right)^{p_{jk}} - K_{r,j} \prod_k \left(a_k \frac{c_k}{1000} \right)^{q_{jk}} \right], \tag{24}$$

where $p_{jk} = \max(s_{jk}, 0)$, $q_{jk} = -\min(s_{jk}, 0)$, while the remaining variables and parameters need to be defined for specific reactions. If the j^{th} reaction occurs in the electrolyte, the variables and parameters are defined in the electrolyte: β_j is the volume fraction of liquid electrolyte (i.e., $\beta_j = \epsilon_l$), and $K_{f,j}$ and $K_{f,j}$ are respectively the forward and reverse reaction rate constants per unit volume of electrolyte. If the j^{th} reaction occurs on a substrate or solid surface, the variables and parameters are defined on the surface: β_j is the reactive surface area (i.e., $\beta_j = A_j$), and $K_{f,j}$ and $K_{f,j}$ are respectively the forward and reverse reaction rate constants on a unit reactive surface area.

2.2.2 Solid- and gas-phase volume evolution

The electrochemical and chemical reactions may modify the solid phase volume fraction (i.e., the ratio of the solid-phase volume to the control volume) in space and time, which is governed by the following equation:

$$\frac{\partial \epsilon_s}{\partial t} + \sum_{k_s} \left(V_{\mathrm{m},k_s} \sum_j S_{k_s j} \right) = 0, \tag{25}$$

where ϵ_s is the solid-phase volume fraction (i.e., the ratio of the gas-phase volume to the control volume) which can be computed from the Boolean model (i.e., $\epsilon_s = \epsilon_0 \left[1 - \exp\left(-\epsilon_s^e/\epsilon_0\right)\right]$), i_s refers to the species forming a solid phase, and V_{m,i_s} is the molar volume of the solid phase. We assume any generated gas phase is non-reactive but can exchange mass with dissolved gas in the electrolyte. The temporal evolution of the gas phase is represented by a first-order-rate model, which yields

$$\frac{\partial \epsilon_g}{\partial t} + \sum_{k_g} V_{\mathrm{m},k_g} Q_{k_g} = 0, \tag{26}$$

where ϵ_g is the gas-phase volume fraction which can also be computed from the Boolean model (i.e., $\epsilon_g = \epsilon_0 \exp\left(-\epsilon_s^e/\epsilon_0\right)\left[1 - \exp\left(-\epsilon_g^e/\epsilon_0\right)\right]$), k_g refers to the species forming a gas phase, V_{m,k_g} is the molar volume of the species k_g in the gas phase, Q_{k_g} is the mass transfer rate between dissolved gas in the liquid electrolyte and the gas phase. We assume Q_{k_g} follows a first-order mass transfer model, i.e., $Q_{k_g} = \kappa_{g,k_g} A_{gl}\left(c_{k_g}^{\mathrm{eq}} - c_{k_g}\right)$, where κ_{g,k_g} is the first-order mass transfer rate constant between dissolved gas and gas phase, $c_{k_g}^{\mathrm{eq}}$ is the equilibrium gas concentration which is assumed to follow Henry's law (i.e., $c_{k_g}^{\mathrm{eq}} = H_{k_g} p_{k_g}$, where H_{k_g} and p_{k_g} are the Henry solubility and partial pressure of component k_g in the gas phase, respectively).

Note that we compute ϵ_s and ϵ_g by representing the solid and gas phases as fully-penetrated hemispheres, and assume the hemispheres grow or shrink at the same rate.

2.2.3 Chemical species and charge transport

In addition to reactions, the chemical species also migrate in the liquid electrolyte. Their transport is governed by diffusion and electrical migration in the electrolyte, represented by the following mass conservation equation:

$$\frac{\partial \epsilon_l c_k}{\partial t} = -\frac{\partial J_k}{\partial x} + \sum_j S_{jk} + Q_k, \tag{27}$$

where ϵ_l is the liquid-phase volume fraction (i.e., $\epsilon_l = \epsilon_0 - \epsilon_s - \epsilon_g$, where ϵ_0, ϵ_s, and ϵ_g are respectively the initial porosity, solid-phase volume fraction, and gas-phase volume fraction.) and J_k is the flux of the k^{th} species (i.e., $J_k = -\epsilon_l D_k\left(\frac{\partial c_k}{\partial x} + \frac{c_k z_k F}{RT}\frac{\partial \phi_l}{\partial x}\right)$, where D_k is the effective diffusivity of the k^{th} species. Here $D_k = \tau D_{0,k}$, where τ is the tortuosity factor and $D_{0,k}$ is the molecular diffusion coefficient in free electrolyte). The transport of ionic species also leads to charge transport in the liquid electrolyte, which is governed by the following equation:

$$\frac{\partial i_l}{\partial x} = \sum_j A_j i_j, \tag{28}$$

where $i_l = F \sum_k z_k J_k$. The charge can also migrate in the solid substrate. We assume that the solid phase remains locally electroneutral and that charge transfer occurs under steady-state conditions. Under these assumptions, solid-phase charge transport is governed by:

$$\frac{\partial i_s}{\partial x} = -\sum_j A_j i_j, \tag{29}$$

where $i_s = -\sigma \frac{\partial \phi_s}{\partial x}$, with σ being the effective conductivity of solid substrate.

Equations (14–29) provide the governing equations for electrochemical and chemical reactions, multispecies ion transport, and charge transport in aqueous batteries. The equations can be solved using the initial and boundary conditions introduced in the following two sections, respectively.

2.2.4 Initial conditions

We present the initial conditions for the charge process, while those for discharge are obtained from the final state of the charge simulation. Any conditions specific to discharge will be described explicitly. We assume the system is in chemical equilibrium at the beginning of charge, and accordingly, the initial ion concentrations and porosities are given by

$$\begin{aligned} c_k(t=0) &= c_{0,k}, \\ \epsilon_s(t=0) &= 0, \\ \epsilon_g(t=0) &= 0, \end{aligned} \tag{30}$$

where $c_{0,k}$ is the initial concentration of the k^{th} species, which is known from experiments.

Additionally, the initial amounts and sizes of solid- and gas-phase hemispheres must be defined. If the electro-deposition and gas generation are initiated by nucleation processes, new hemispheres (i.e., nuclei) can form at any time, and the quantity of new hemispheres is determined via Equation (20). New hemispheres start with zero size and subsequently grow through electro-deposition. Conversely, the quantity of pre-existing hemispheres remains

constant over time, but their sizes continue to increase. The growth rates are calculated using the methods outlined at the end of Section 2.2.1. Note that the electro-dissolution discharge simulations only need the initial numbers and sizes of the solid-phase and gas-phase hemispheres, since no new hemispheres are being generated.

2.2.5 Boundary conditions

We consider two types of boundary conditions for our simulations: applied current and applied voltage.

Applied current Suppose the current density $i_{\text{tot}}(t)$ is applied to a cell with length L, defined by $L = L_a + L_{sp} + L_c$ where L_a, L_{sp}, and L_c are respectively the lengths of the negative electrode (referred to as "anode" hereafter), separator, and positive electrode (referred to as "cathode" hereafter). The boundary conditions at the interfaces between the current collector and the anode ($x = 0$) and the cathode ($x = L$) are given by:

$$-\sigma \frac{\partial \phi_s}{\partial x}\Big|_{x=0} = -\sigma \frac{\partial \phi_s}{\partial x}\Big|_{x=L} = i_{\text{tot}}(t), \tag{31}$$

where $i_{\text{tot}}(t)$ is the area-specific current applied to or generated by the battery cell at time t. Ions cannot penetrate the current collectors, and therefore the ion fluxes at the interface between the current collector and the anode ($x = 0$) or cathode ($x = L$) are zero, which yields

$$J_k|_{x=0} = J_k|_{x=L} = 0. \tag{32}$$

Correspondingly, the gradient of the liquid-phase electropotential is zero at $x = 0$ and $x = L$. Here, instead of using $\frac{\partial \phi_l}{\partial x}|_{x=0} = 0$, we set $\phi_l(x = 0) = 0$ such that $\phi_l(x)$ elsewhere has a common reference point. Therefore, the boundary conditions for the liquid-phase charge transport are given by

$$\phi_l|_{x=0} = 0, \quad \text{and} \quad \frac{\partial \phi_l}{\partial x}\Big|_{x=L} = 0. \tag{33}$$

Additionally, the insulating separator yields zero electron flux at the interfaces between the separator and anode ($x = L_a$) and cathode ($x = L_a + L_{sp}$), which leads to

$$\left.\frac{\partial \phi_s}{\partial x}\right|_{x=L_a} = \left.\frac{\partial \phi_s}{\partial x}\right|_{x=L_a+L_{sp}} = 0. \tag{34}$$

Applied voltage When a voltage $V_0(t)$ is applied to the cell, the boundary conditions remain the same, except for Equation (31). The equation becomes

$$\begin{aligned} \phi_s|_{x=L} - \phi_s|_{x=0} &= V_0(t), \\ \left.\frac{\partial \phi_s}{\partial x}\right|_{x=L} - \left.\frac{\partial \phi_s}{\partial x}\right|_{x=0} &= 0, \end{aligned} \tag{35}$$

where $V_0(t)$ is the voltage applied to, or generated by, the battery cell at time t. Equation (35) represents an applied external voltage and a global charge conservation.

2.3 Numerical algorithm

Equations (14–29) represent the governing equations of the mathematical model for reactions, ion transport, and charge transport processes in an aqueous battery cell. The equations have the following unknown primary variables: ion concentrations c_i, liquid-phase potential ϕ_l, solid-phase potential ϕ_s, solid-phase volume fraction ϵ_s, and gas-phase volume fraction ϵ_g. The primary variables can be solved numerically by imposing the initial conditions (i.e., Equation (30)) and boundary conditions (i.e., Equations (32–35)). Here, this is done by first discretizing the governing equations in space using a finite volume method and in time using a backward-Euler method. Then, the resulting nonlinear discretized equations are solved by a quasi-Newton method given that a standard Newton-Raphson method is challenged by the exponential relationship between the electrochemical reaction rates and the overpotential, which is a function of ϕ_s and ϕ_l (see Equation (15)). In particular, if the initial guesses for ϕ_s and ϕ_l are not close enough to the solutions, their absolute values may become excessively large, leading to reaction rates that exceed floating-point limits and Newton iterations that

do not converge. The adopted quasi-Newton method addresses this challenge by replacing the exponential terms in Equation (15) by their truncated Taylor series and solving the approximated equations for the first time step. We then use the approximate solutions as initial guesses and resolve the original equations for the same time step. Once the solution is obtained, we can solve the original equations for the subsequent time steps. We note that the truncation order of the Taylor series may need to be adjusted for different simulations, and more advanced methods (e.g., similarity variable method) may be used for solving the nonlinear model.

2.4 Model evaluation

We evaluate the model by simulating the potentiostatic and galvanostatic charge–discharge curves of three aqueous battery chemistries: (1) acidic H_2–Mn, (2) near-neutral Zn–MnO_2, and (3) alkaline Sn–NiOOH.

2.4.1 Data collection

We first collect experimental data sets from the literature for acidic H_2–Mn [20] and near-neutral Zn–MnO_2 [31] batteries and measure those for the alkaline Sn–NiOOH battery through laboratory experiments.

The acidic H_2–Mn battery data was initially reported by Chen et al. [20]. Their experiments were performed in Swagelok cells that consist of a MnO_2 cathode, a Pt/C-coated anode, a glass fiber separator, and a $MnSO_4$ and H_2SO_4 electrolyte (see Table S2). The cells were charged at constant voltage to four different cell capacities, and then discharged at the same rate (see Table S3).

The near-neutral Zn–MnO_2 battery data was reported by Zhou et al. [31], who utilized pouch cells with a MnO_2-based cathode, a Zn foam-based anode, a glass fiber separator, and an aqueous solution of $ZnSO_4$ and $MnSO_4$ as the electrolyte (see Table S2). The charge–discharge curves were collected for five different current densities across a fixed voltage range,

corresponding to five capacities (see Table S3).

Finally, we constructed alkaline Sn–NiOOH battery pouch cells in an "anode free" configuration, using two anode substrates (copper foam and carbon felt), $Ni(OH)_2$ cathodes, monovalent anion-exchange membrane separators, and an aqueous solution of $K_2Sn(OH)_6$ and KOH as the electrolyte (see Table S2). We measure galvanostatic charge–discharge curves at different applied current densities (see Table S3).

2.4.2 Model parameter calibration

The collected data sets are then used to calibrate the model parameters to simulate the charge–discharge curves for all three aqueous battery chemistries. While some parameters (e.g., cell dimensions, material properties, and electrolyte compositions) were provided based on reported measurements, others were calibrated using experimental data. For all chemistries investigated, we assume the charge transfer coefficient to be 0.5[11]. We manually tuned the rest of the unknown parameters by fitting the model to a single experimental charge and discharge curve and then evaluated the validity and accuracy of the model using the remaining charge and discharge curves. The tuning parameters for each battery configuration are specified in Section 3.

2.4.3 Model parameter sensitivity analysis

We also quantify the individual and combined effects of model parameters on model performance using a global sensitivity analysis known as the Sobol method[32,33]. Briefly, the Sobol method begins by defining the number of model parameters (N_p) and their associated ranges. These vary across different aqueous batteries and will be specified in Section 3, where the Sobol analysis is applied. The parameters are either constrained by known physical ranges or, when uncertain, assumed to be bounded between one-tenth and ten times the best-fitted values. We then run $N_s \times (N_p + 2)$ Monte Carlo simulations using parameter sets randomly sampled from their ranges via a Sobol quasi-random sequence. Here N_s is the number of

samples for each parameter, which is set to 1,024[32,33]. For each parameter set, we run model simulations under all experimental conditions and compute the mean root-mean-square error (RMSE) across all simulated curves. Finally, we use the mean RMSE as the model performance metric to evaluate both the sensitivity of individual parameters (i.e., first-order Sobol index) and the combined effects of parameter pairs (i.e., second-order Sobol index).

3 Results and analysis

3.1 Model evaluation and validation

We apply the model described in Sections 2.2–2.3 to simulate the charge–discharge curves for the acidic H_2–Mn, near-neutral Zn–MnO_2, and alkaline Sn–NiOOH aqueous battery cells. The modeling results are evaluated and validated using the data collected in Section 2.4. The modeling results and analysis are discussed in the following sections.

3.1.1 Modeling potentiostatic charge and galvanostatic discharge curves of an acidic H_2–Mn battery

We first evaluate the model by simulating the potentiostatic charge and galvanostatic discharge curves for the acidic H_2–Mn battery[20] (see the reaction schematic in Figure 3a–b and reactions in Equations (1–2)). The model parameters for cell dimensions and electrode material properties are summarized in Table S4. We calibrate three unknown parameters (i.e., the exchange current density of the anode reaction, and the initial reactive surface areas of the anode and cathode substrates) using one experimental dataset where the cell is charged at $V_0(t)$=1.6 V to 20 mAh, and then discharged at $i_{tot}(t) = 10\,mA/cm^2$. The parameters are tuned until a good match is reached between the simulation results and experimental data, and then the calibrated model is applied to simulate the remaining three charge–discharge curves. As shown in Figure 3c, the modeled curves present an excellent match to the measured ones as evidenced by the small root-mean-square errors (RMSE =

0.025 V $\sim$ 0.046 V).

A closer inspection reveals nonuniform ion concentrations and pH across the cell and nonuniform electro-deposition of MnO_2 across the cathode during the charge–discharge cycles (Figures 3d–g and S2). This indicates that the reactant transport is slower than the electrochemical reactions and is the rate-limiting process in the system. We examine the relative importance of ion transport and electrochemical reaction by computing the Damköhler number defined by $Da = \frac{L^2 \kappa_{jk}}{\bar{D}_i}$, where i refers to the controlling reactant (i.e., k= Mn^{2+} or H^+ during charge, while i= Mn^{2+} or H_2 during discharge), κ_{jk} refers to the rate constant of the controlling reaction (i.e., κ_{jk} is estimated by $\bar{S}_{jk}/\bar{c}_i$ where $\bar{S}_{jk}$ and $\bar{c}_i$ are the representative reaction rate and concentration and are estimated by domain-averaged reaction rate and concentration at the beginning of the simulations), and $\bar{D}_i$ is the effective diffusivity (i.e., $\bar{D}_i = (L_a\epsilon_a D_{a,i} + L_{sp}\epsilon_{sp} D_{sep,i} + L_c\epsilon_c D_{c,i})/(L_a\epsilon_a + L_{sp}\epsilon_{sp} + L_c\epsilon_c)$). If $Da \gg 1$, the system is transport-controlled. In contrast, if $Da \ll 1$, the system is reaction-controlled. The calculations yield $Da = 1.1 \times 10^3 \sim 1.5 \times 10^4$ during charge, verifying a transport-controlled system. We acknowledge that the current experiments fall in the low-utilization regimes where less than 5.3% Mn^{2+} is participating in the electrochemical reactions, and thus the system has sufficient Mn^{2+} for electrochemical reactions during the charge and discharge cycles. Therefore, no significant transport-limited behavior is observed during discharge.

To further identify the dominant controlling factors, we perform a global sensitivity analysis on the following three uncertain parameters: the anode exchange current density ($i_{0,1}$), the initial anode reactive surface area ($A_{0,\mathrm{an}}$), and the initial cathode reactive surface area ($A_{0,\mathrm{ca}}$) (Figure S6). The results indicate that model performance is primarily governed by the anode reaction parameters (particularly $A_{0,\mathrm{an}}$, which has a first-order Sobol index of 0.87), whereas the cathode reactive surface area exerts only a minor influence. This finding indicates that the system is within the low MnO_2 utilization regime and that anode processes controls the overall cell overpotential.

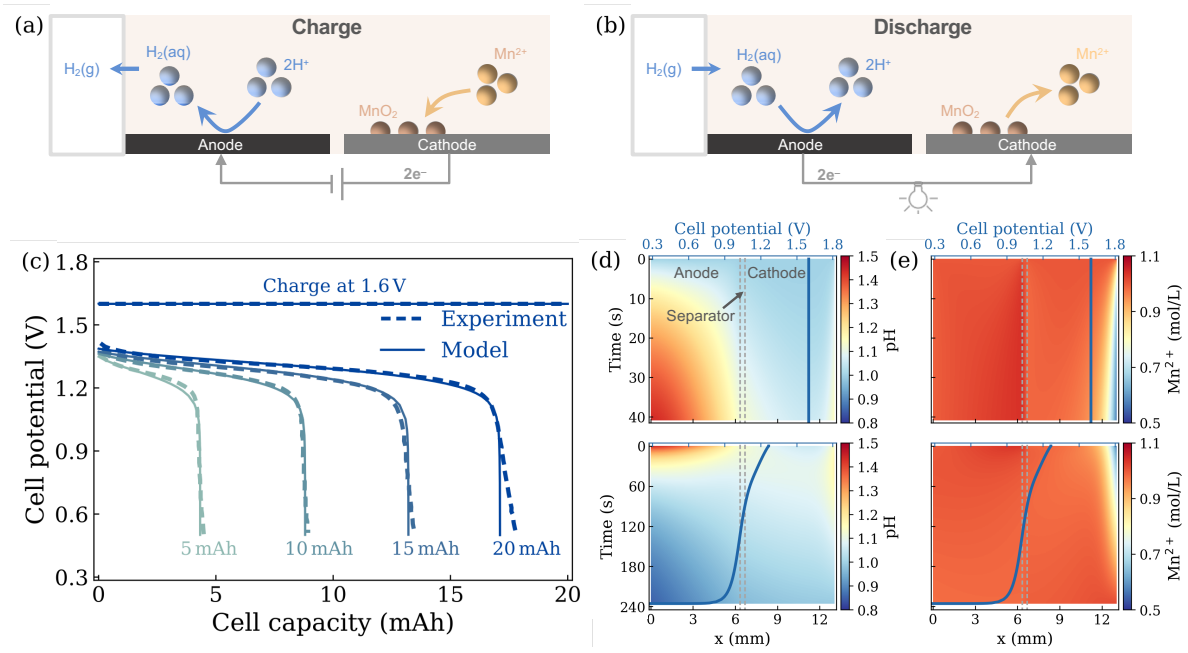

Figure 3: (a–b) Conceptual model representation of the charge and discharge of an acidic H_2–Mn battery. (c) Modeled vs. measured potentiostatic charge and galvanostatic discharge curves of an acidic H_2–Mn battery cell. The cell is charged at a constant voltage (i.e., $V_0(t)$=1.6 V) to a certain capacity (i.e., 5, 10, 15, or 20 mAh), and then discharged at four current densities (i.e., $i_{tot}(t) = 10\,mA/cm^2$). The experimental data are collected from the work of Chen et al.[20]. Note that because the cell was charged to different capacities in the experiments and its charge curves overlapped, we present the curve that reaches the largest capacity. The corresponding charge curve for the electric current is provided in Figure S1. Spatial and temporal variations of (d) pH and (e) Mn^{2+} concentration during the charge (top row of Panels d–e) and discharge (bottom row of Panels d–e) of an acidic H_2–Mn battery with a cycle capacity of 1 mAh at a constant charge voltage (1.6 V) and a discharge rate of $10\,mA/cm^2$. During discharge, the initial ion concentration and MnO_2 profiles are the same as those at the end of charge. The gray dashed lines indicate the boundary between the anode and the separator (left) and the boundary between the separator and the cathode (right).

3.1.2 Modeling galvanostatic curves of a near-neutral Zn–MnO_2 battery

Next, we evaluate the model by simulating the galvanostatic charge–discharge curves for the near-neutral Zn–MnO_2 battery from reported experiments[31], which probed the performance of the system under rates ranging from 1 C to 30 C (Here 1 C refers to the rate at which a battery cell is fully charged or discharged in 1 hour). The governing equations of the near-

neutral Zn–MnO_2 battery are described in Equation (4) and Equations (5–7) for the anode and cathode, respectively. To parameterize the model, we make the following assumptions: (1) In the electrolyte, water dissociation is in chemical equilibrium (i.e., $\mathrm{pH} + \mathrm{pOH} = 14$). (2) In the anode, Zn deposition/dissolution is treated as the primary reaction, while side reactions such as H_2 evolution and ZHS formation/dissolution are not explicitly included. The solid-phase Zn is also represented by a group of equal-size hemispheres rather than a distribution of varying-size hemispheres, and the Zn surface area is calculated using the Boolean model. These simplifications are adopted because the simulated cell has an oversized Zn anode relative to the MnO_2 cathode, such that anode-side side reactions and detailed Zn morphology evolution are expected to have only a minor influence on the reported charge–discharge curves. In other systems or under different conditions, these processes may need to be considered explicitly. (3) In the MnO_2 cathode, we assume Zn^{2+} and H^+ independently intercalate into or deintercalate from MnO_2 (i.e., a fraction of MnO_2 is used for Zn^{2+} (de)intercalation, while the remaining is used for H^+ (de)intercalation). (4) The Zn^{2+} and H^+ (de)intercalation reactions are modeled by the following modified Butler-Volmer equations:

$$\begin{aligned} i_2 &= i_{0,2}\left[(1-\mathrm{SOC}_{\mathrm{Zn^{2+}}})\left(\frac{c_{\mathrm{Zn^{2+}}}}{1000}\right)^{1/2}\exp\left(\frac{\alpha_{a2}F}{R_gT}\eta_2\right) - \mathrm{SOC}_{\mathrm{Zn^{2+}}}\exp\left(-\frac{\alpha_{c2}F}{R_gT}\eta_2\right)\right], \\ i_3 &= i_{0,3}\left[(1-\mathrm{SOC}_{\mathrm{H^{+}}})\left(\frac{c_{\mathrm{H+}}}{1000}\right)\exp\left(\frac{\alpha_{a3}F}{R_gT}\eta_3\right) - \mathrm{SOC}_{\mathrm{H^{+}}}\exp\left(-\frac{\alpha_{c3}F}{R_gT}\eta_3\right)\right], \end{aligned} \tag{36}$$

where i_2 and i_3 respectively denote the exchange current densities for Zn^{2+} and H^+ (de)intercalation reactions (where we keep the subscripts consistent with the reaction indexes presented in Section 2.1.2), $\mathrm{SOC}_{\mathrm{Zn^{2+}}}$ denotes the state of charge at Zn^{2+} (de)intercalation sites (i.e., $\mathrm{SOC}_{\mathrm{Zn^{2+}}} = c_{s,\mathrm{Zn^{2+}}}/c^{\mathrm{m}}_{s,\mathrm{Zn^{2+}}}$ with $c_{s,\mathrm{Zn^{2+}}}$ being the solid-phase Zn^{2+} concentration and $c^{\mathrm{m}}_{s,\mathrm{Zn^{2+}}}$ being the maximum solid-phase Zn^{2+} concentration), $\mathrm{SOC}_{\mathrm{H^{+}}}$ denotes the state of charge at H^+ (de)intercalation sites (i.e., $\mathrm{SOC}_{\mathrm{H^{+}}} = c_{s,\mathrm{H^{+}}}/c^{\mathrm{m}}_{s,\mathrm{H^{+}}}$ with $c_{s,\mathrm{H^{+}}}$ being the solid-phase H^+ concentration and $c^{\mathrm{m}}_{s,\mathrm{H^{+}}}$ being the maximum solid-phase H^+ concentration), and the remaining parameters are defined in Equation (15).

To set up the simulations, we first split the MnO_2 into two types of (de)intercalation sites—which are assigned to Zn^{2+} and H^+—associated with the upper and lower discharge plateaus, respectively. We use the model parameters for cell dimensions and electrode material properties as shown in Table S4, and calibrate the eleven remaining unknown parameters—the initial number and size of Zn hemispheres, the standard potential for two (de)intercalation reactions ($U_{\theta,j}$), the exchange current densities for all reactions ($i_{0,j}$), the reaction rate constants for all chemical reactions (K_f and K_r), the initial reactive substrate surface area of the cathode reaction ($A_{0,\mathrm{ca}}$)—using one experimental data set where the cell is cycled at 1 C. This calibration is then used to predict the other voltage curves.

We observe that the model predictions deviate from the experimental data (Figure S3). This deviation is likely due to the neglect of solid-phase diffusion processes and their impact on active material accessibility and cell capacity at higher rates. To account for the rate-dependent cell capacities, we introduce a threshold for the available MnO_2 (i.e., maximum saturation of Zn^{2+} and H^+ in the MnO_2). Because the threshold is rate-dependent, we calibrate its value for each rate using the following procedure. At a targeted rate, we first approximate the available MnO_2 threshold by the ratio between the measured capacity and the theoretical capacity. We then recalibrate all the model parameters for the discharge curve and use the recalibrated model to predict the charge curve at the same rate. As shown in Figure 4a, the modeled charge–discharge curves show a much better match with the measured ones as demonstrated by the low root-mean-square errors—RMSE =0.012 V$\sim$0.086 V for the charge curves, and RMSE = 0.035 V$\sim$0.052 V for the discharge curves. The agreement between the simulations and measurements validates the new model parameterization. A closer look shows that the spatial profiles of ion concentrations and pH are uniform across the cell (Figure 5). Additionally, the Damköhler numbers range from 2.1×10^{-3} to 2.2. Both the uniform ion concentration profiles and smaller Damköhler numbers indicate that the system is not limited by ion transport, but controlled instead by the electrochemical reactions.

We compute the electrode-averaged properties to examine the controlling factors of the

charge–discharge behavior with particular emphasis on the two discharge plateaus—a critical process that extends the utilization of MnO_2. Our simulations indicate that the first discharge plateau is dominated by Zn^{2+} intercalation in the MnO_2 cathode (Equation (5)), which has a higher equilibrium redox potential. When the MnO_2 cannot accommodate further Zn^{2+} intercalation, the second reaction (i.e., H^+ intercalation) becomes the dominant process. Additionally, voltage rebound is observed, which we attribute to the competition between H^+ intercalation (Equation (6)) and $Zn_4SO_4(OH)_6 \cdot xH_2O$(s) (ZHS) precipitation (Equation (7)). As H^+ intercalation becomes the dominant electrochemical reaction, the pH increases rapidly, but is then counterbalanced by the precipitation of ZHS, which consumes OH^- and maintains the near-neutral condition (Figure 4). This sustains the H^+ concentration and the higher voltage during the 2^{nd}-stage discharge. Finally, at the end of the 2^{nd}-stage discharge, the depletion of intercalation sites within MnO_2 becomes dominant and lowers the voltage (Figure 4c).

Given that the battery behavior is primarily controlled by cathode processes, we examine the key controlling factors via a global sensitivity analysis (i.e., Sobol's method) on the following uncertain cathode reaction parameters: the total available MnO_2 for (de)intercalation reactions ($M^{\text{In}}_{Zn^{2+}} + M^{\text{In}}_{H^+}$), the fraction of Zn^{2+} (de)intercalation sites ($M^{\text{In}}_{Zn^{2+}}/M^{\text{In}}_{H^+}$), the initial cathode reaction area ($A_{0,\text{ca}}$), the exchange current density for Zn^{2+} (de)intercalation ($i_{0,2}$), the exchange current density for H^+ (de)intercalation ($i_{0,3}$), and the forward and reverse reaction rate constant for ZHS deposition/dissolution ($K_{f,\text{ca}}$ and $K_{r,\text{ca}}$) (Figure S7). The results show that $M^{\text{In}}_{Zn^{2+}} + M^{\text{In}}_{H^+}$ has the greatest first-order Sobol index (0.58) and serves as the major controlling factor of the simulated charge and discharge behaviors, which further highlights the need to capture the rate-dependent capacities.

We note that the simulated reactions follow hypotheses (i.e., Zn^{2+} (de)intercalation, H^+ (de)intercalation, and ZHS precipitation/dissolution) that have been partly verified by experimental observations such as operando X-ray crystallography, scanning electron microscopy, and X-ray computed tomography[21]. We will discuss other existing hypotheses and explain

how the modeling study can advance our understanding and investigation of near-neutral Zn–MnO_2 battery systems in Section 4.

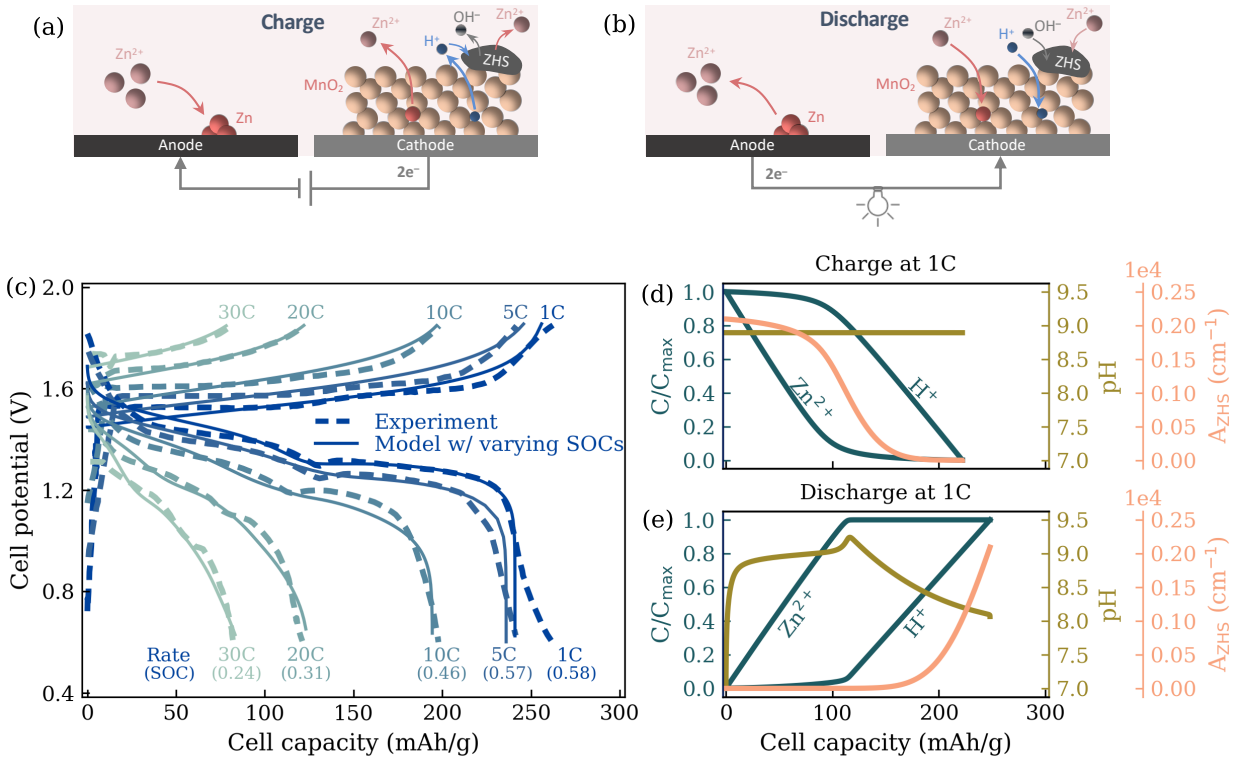

Figure 4: (a–b) Conceptual model representation of the charge and discharge of a near-neutral Zn–MnO_2 battery. (c) Modeled vs. measured galvanostatic charge–discharge curves of a near-neutral Zn–MnO_2 battery cell. The cell is charged and discharged at five current densities (i.e., $i_{\text{tot}}(\text{t}) = 1$, 5, 10, 20, and 30 C where 1 C = 308 mA/g, where 1 C refers to the rate at which a battery cell is fully charged or discharged in 1 hour). The experimental data are collected from the work of Zhou et al.[31]. (d–e) We present the intercalated Zn^{2+} concentration in the MnO_2 (normalized by the maximum amount of intercalation sites for Zn^{2+} intercalation), the intercalated H^+ concentration in the MnO_2 (normalized by the maximum amount of intercalation sites for H^+ intercalations), pH, and the surface areas of $Zn_4SO_4(OH)_6 \cdot xH_2O$(s) (ZHS) during the (d) charge and (e) discharge at $i_{\text{tot}}(\text{t}) = 1$ C. Note that in order to capture the rate-dependent cell capacities, the model needs to set different maximum saturations of Zn^{2+} and H^+ in the MnO_2 (i.e., state of charge or SOC) in different simulations. Here we set SOCs to 0.58, 0.57, 0.46, 0.31, and 0.24.

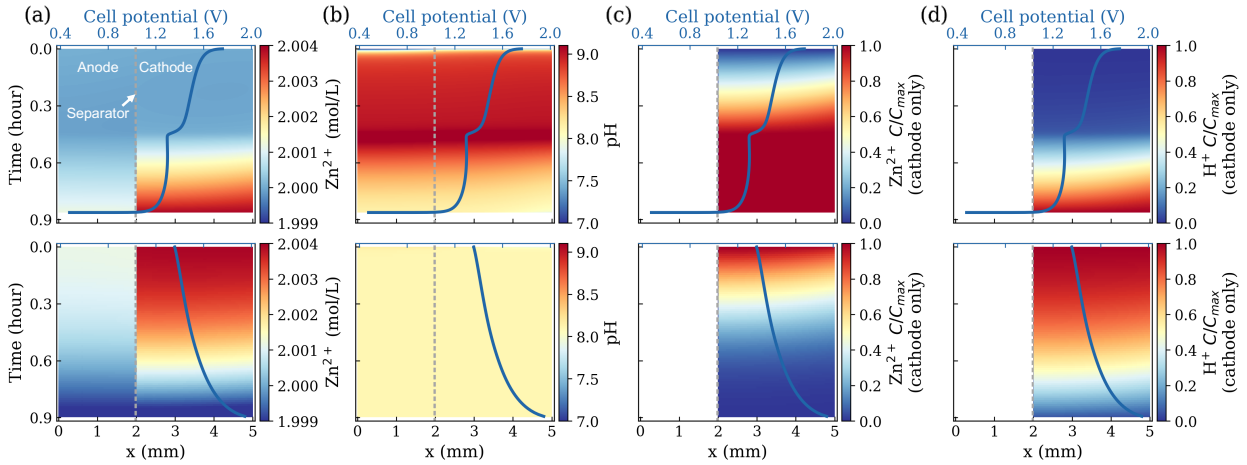

Figure 5: Spatial and temporal variations in (a) aqueous Zn^{2+} concentration, (b) pH, (c) Zn^{2+} concentration in MnO_2, and (d) H^+ concentration in MnO_2 during the charge (top row) and discharge (bottom row) of an Zn-MnO_2 battery cell. Note that because the Zn-MnO_2 battery cells are assembled and tested from a fully charged state in the experiments, the simulations begin from discharge and are followed by charge. For demonstration purposes, we present the simulation results for a capacity of 308 mA/g and a rate of 1 C. The left gray dashed line indicates the boundary between the anode and the separator, while the right gray dashed line indicates the boundary between the separator and the cathode.

3.1.3 Modeling galvanostatic curves of an alkaline Sn–NiOOH battery

As the third and final case, we benchmark the model by simulating the galvanostatic charge–discharge curves for the alkaline Sn–NiOOH battery using a copper anode substrate (Equations (8–10)) and (Equations (11–12)) for the anode and cathode, respectively.

We simulate four charge–discharge curves for two capacities and four rates, where a 1.286 mAh cell is charged and discharged at two lower rates (0.05 mA/cm^2 and 0.1 mA/cm^2), and a 2 mAh cell is charged and discharged at two higher rates (0.5 mA/cm^2 and 1 mA/cm^2). Similar to the prior simulations, we first use one experimental dataset where the cell is charged and discharged at $i_{\text{tot}}(\text{t}) = 1$ mA/cm^2 for a capacity of 2 mAh to determine the nine unknown parameters—the exchange current densities for the anode electrochemical reactions ($i_{0,j}$), the reaction rate constants for all chemical reactions (K_f and K_r), initial reactive substrate surface area for the anode reaction (A_0), and nucleation parameters (Z_{jk} and f_{jk}). Because the electro-deposited Sn solids on copper surfaces are uniform and non-spherical[5],

we also tune the scalar for Sn solid surface area (λ_{sl}) and the scalar Sn–copper interfacial area (λ_{ss}). While the parameters for cell dimensions and electrode material properties are shown in Table S4, the calibrated parameters are reported in Tables S5, S6, and S7.

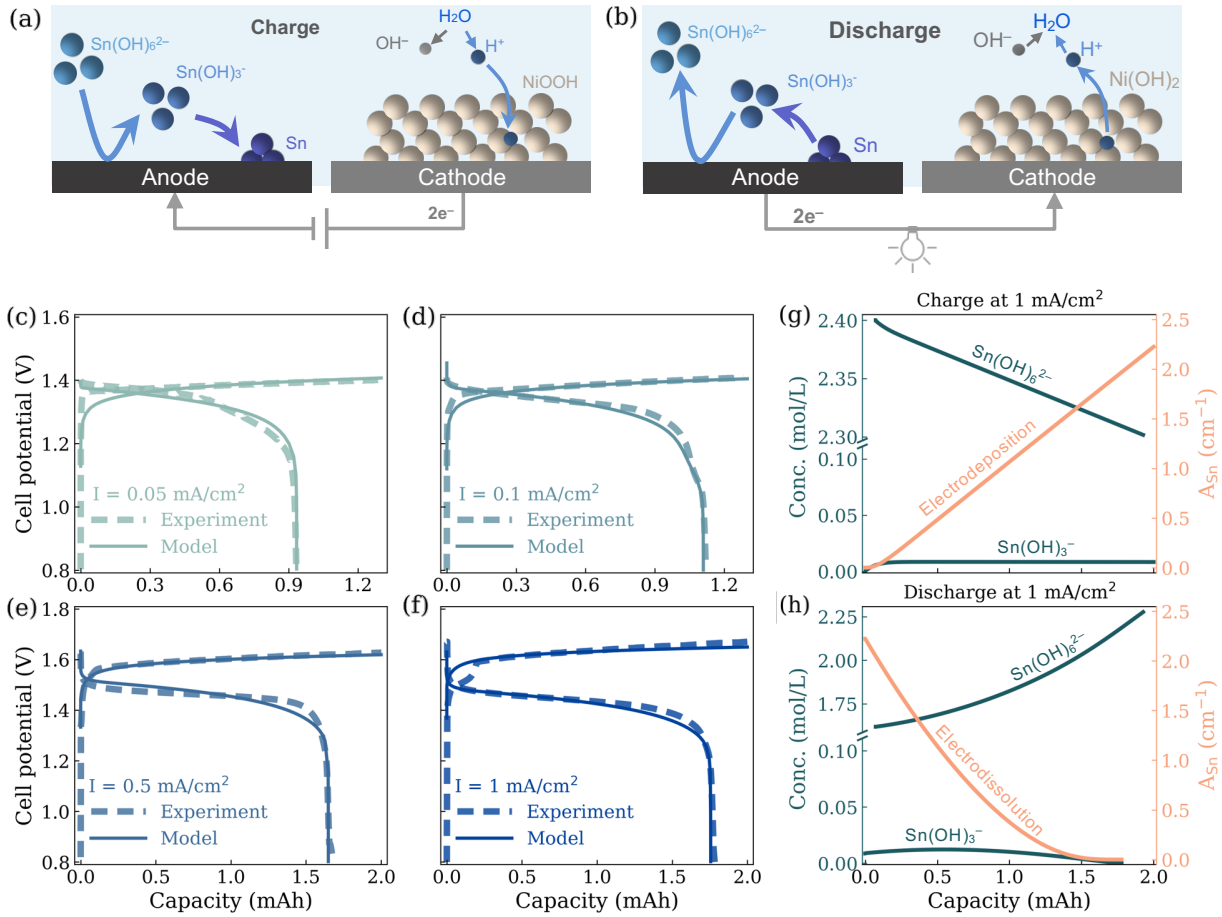

Figure 6: (a–b) Conceptual model representation of the charge and discharge of an alkaline Sn–NiOOH battery cell. (c–f) Modeled vs. measured galvanostatic charge and discharge curves of an alkaline Sn–NiOOH battery cell using a copper-based anode and an anion exchange membrane as the separator. The cells have two cycling capacities (i.e., 1.286 and 2 mAh). The cell with a lower capacity is charged and discharged at 0.05 and 0.1 mA/cm^2, while the one with a higher capacity is charged and discharged at 0.5 and 1 mA/cm^2. (g–h) The temporal evolutions of the electrode-averaged $Sn(OH)_3^-$ concentration, $Sn(OH)_6^{2-}$ concentration, and solid Sn surface area during the (g) charge and (h) discharge of the 2 mAh cell at $i_{tot}(t) = 1$ mA/cm^2.

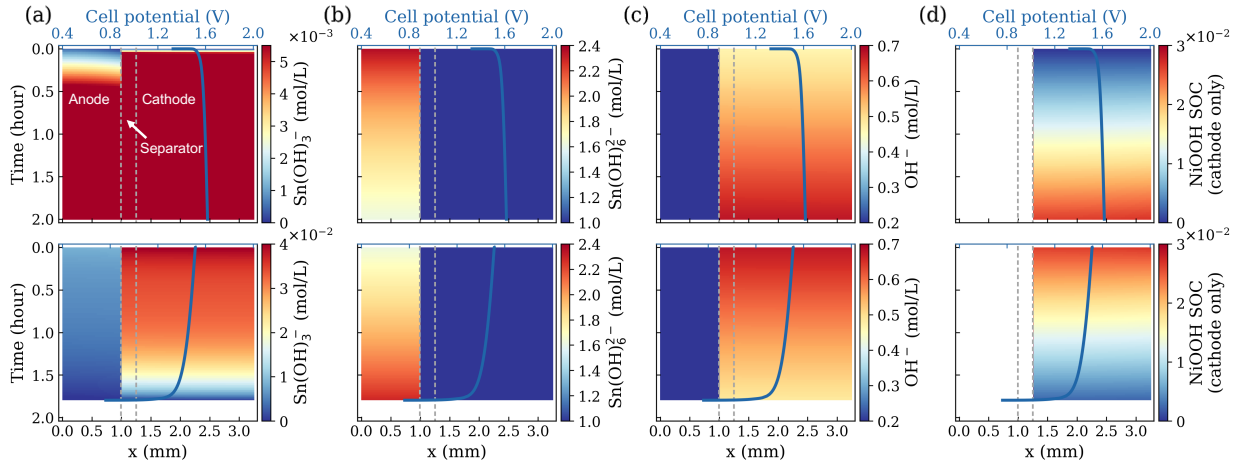

Figure 7: Spatial and temporal variations of (a) $Sn(OH)_3^-$ concentration, (b) $Sn(OH)_6^{2-}$ concentration, (c) OH^- concentration, and (d) cathode state of charge (i.e., the mole fraction of NiOOH) during the charge (top row) and discharge (bottom row) of an alkaline Sn-NiOOH battery cell using a copper-based anode substrate. For demonstration purposes, we present the simulation results for a capacity of 2 mAh and a rate of 1 mA/cm^2. The left gray dashed line indicates the boundary between the anode and the separator, while the right gray dashed line indicates the boundary between the separator and the cathode. Note that as the cell is constructed with separate negative and positive electrolytes and uses a monovalent anion exchange membrane as a separator, $Sn(OH)_6^{2-}$ is constrained to the anode and therefore its concentration is near zero within the separator and cathode (indicated by the blue color).

The calibrated model is then applied to simulate the remaining three charge–discharge curves. As shown in Figure 6a–d, the model reproduces the measured charge–discharge curves—the root-mean-square errors are 0.013 V∼0.027 V for the charge curves and 0.016 V∼0.038 V for the discharge curves. Both measured and modeled discharge curves show a single voltage plateau for the charge and discharge processes (Figure 6f), despite the occurrence of two subsequent reactions—a faster 1st-step Sn electrodissolution reaction and a slower 2nd-step $Sn(OH)_3^-$ oxidation reaction (Figure 6f). This is because the two reactions share similar equilibrium redox potentials as well as similar reaction kinetics on the copper substrate[4,34]. Figure S4 shows the model response when the discharge is simulated as a single-step reaction. This simplification leads to substantially worse agreement with experiments as the model overestimates the discharge capacity due to the exclusion of the chemical self-discharge pathway involving the $Sn(OH)_3^-$ intermediate.

Similar to the Zn-MnO_2 system, the cell charge–discharge performance is mainly controlled by electrochemical reactions as suggested by the uniform ion concentration profiles (Figure 7) and smaller Damköhler numbers ($Da = 1.5\times10^{-3} \sim 3.1\times10^{-3}$). Additionally, we observe that the intermediate product ($Sn(OH)_3^-$) concentrations remain low during charge and discharge due to the low utilization of $Sn(OH)_6^{2-}$ (Figure 6e–f).

We also examine the key controlling factors via a global sensitivity analysis on the following uncertain reaction parameters: the initial reactive surface area in the anode substrate ($A_{0,an}$), the exchange current density for $Sn(s) \leftrightarrow Sn(OH)_3^-$ reaction ($i_{0,1}$), the exchange current density for $Sn(OH)_3^- \leftrightarrow Sn(OH)_6^{2-}$ reaction ($i_{0,2}$), the initial reactive surface area in the cathode substrate ($A_{0,ca}$), the reaction rate constant for the $Sn(OH)_3^-$ disproportionation reaction (K_{an}), and the reaction rate constant for the $Sn(OH)_3^-$ self-discharge reaction (K_{ca}) (Figure S8). The results suggest that $A_{0,an}$, $i_{0,1}$, and their combined effect play the dominant role—their first- and second-order Sobol's indices add up to 0.92. This verifies that the system is primarily controlled by anode processes and highlights the need to characterize the reactive surface area for better predicting the charge-discharge behaviors.

3.2 Model extension

We further demonstrate the model's capability and generalizability by simulating the galvanostatic charge–discharge curves of a technologically-relevant alkaline Sn–NiOOH aqueous battery utilizing a lower-cost carbon-based anode substrate. While the cell structure resembles that of the copper-substrate battery, the electrochemical reactions on the carbon surfaces are more complex[4,34]. Experiments showed that the carbon-substrate significantly alters the charge–discharge behavior, introducing an initial voltage peak during charge and two distinct voltage plateaus during discharge[34]. These observations cannot be captured by the calibrated model obtained in Section 3.1.3 (Figure 8a); therefore, we need to either retune the model parameters or extend the model by considering additional physical processes.

First, we recalibrate the nucleation model parameters by decreasing the nucleation rate

constants (i.e., Z_{jk} and f_{jk}) given that the initial voltage peak potentially indicates a greater energy barrier for nucleation on carbon surfaces (see parameters in Table S7). The recalibrated model ("Model - Nucleation" in Figure 8a) presents a better match with experimental data as evidenced by the decrease of RMSE from 0.063 V to 0.036 V. A closer analysis of the the temporal evolution of the volumes and surface areas of nuclei reveals that current is primarily driven by the reduction of $Sn(OH)_6^{2-}$ to $Sn(OH)_3^-$ (Equation (9)) before the nucleation peak, while plating (Equation (8)) dominates afterwards (Figure 8b). These findings highlight the necessity of incorporating nucleation processes and two-stage reactions to accurately model the plating behavior of Sn on a carbon substrate.

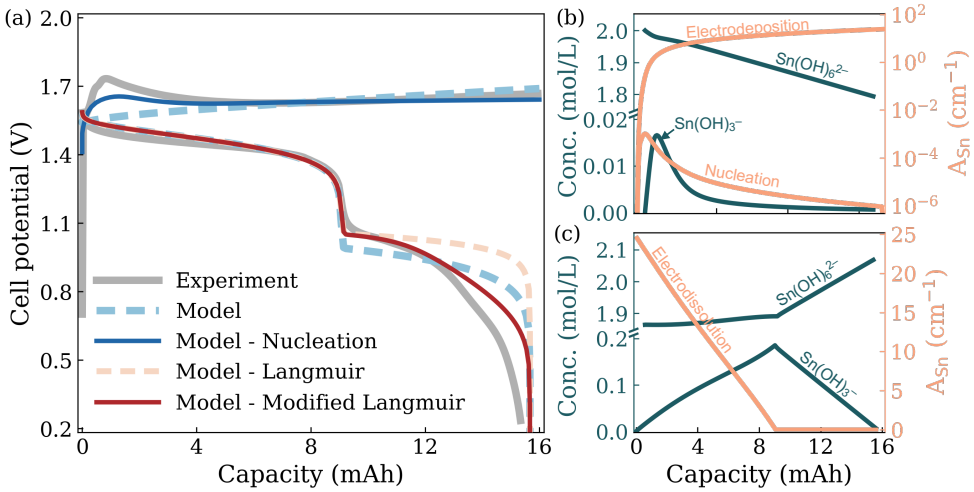

Figure 8: (a) Model extension to simulate the galvanostatic charge–discharge curves of an alkaline Sn–NiOOH battery cell with a carbon-based anode and anion exchange membrane. We compare experimental charge–discharge curves at a current density of 4 mA/cm^2 with simulation results from a model neglecting nucleation for charge and adsorption for discharge (denoted by "Model") and three extended models that account for these phenomena. The first extended model accounts for nucleation and is used for the charge simulation (denoted by "Model - Nucleation"). The second and third extended models account for the adsorption of $Sn(OH)_3^-$ on carbon surfaces—the second couples a standard Langmuir isotherm (denoted by "Model - Langmuir"), while the third incorporates a modified Langmuir isotherm (denoted by "Model - Modified Langmuir"). We also compare the electrode-averaged $Sn(OH)_3^-$ concentration, $Sn(OH)_6^{2-}$ concentration, and solid Sn surface area during (b) charge and (c) discharge.

While the model accurately predicts the 1st-stage discharge voltage plateau, it overestimates the voltage during the 2nd-stage discharge (Figure 8a). The significant voltage loss

suggests an significant overpotential for $Sn(OH)_3^-$ oxidation on carbon surfaces during discharge. In particular, the overpotential may arise from the electrical double layer effect and adsorption enthalpy, which causes the concentration of $Sn(OH)_3^-$ on the carbon surface to deviate from its bulk concentration. To account for the electrical double layer effect and adsorption enthalpy, we extend the model by incorporating a Langmuir-type adsorption model,

$$c_{sf,\mathrm{SnII}} = c^{\mathrm{m}}_{sf,\mathrm{SnII}} \frac{K_{\mathrm{eq}} c_{\mathrm{SnII}}}{1 + K_{\mathrm{eq}} c_{\mathrm{SnII}}}, \tag{37}$$

where $c_{sf,\mathrm{SnII}}$ is the $Sn(OH)_3^-$ concentration on the substrate surface and $c^{\mathrm{m}}_{sf,\mathrm{SnII}}$ is the maximum surface concentration. We implement two models: (1) a standard Langmuir isotherm ("Model - Langmuir"), i.e., $K_{\mathrm{eq}} = \exp\left(-\frac{\Delta G^0_{\mathrm{ads}}}{R_g T}\right) \exp\left(-\frac{z_{\mathrm{SnII}} F \Delta\phi}{R_g T}\right)$[35], where $\Delta G^0_{\mathrm{ads}}$ is the standard Gibbs free energy of chemical adsorption and $\Delta\phi = \phi_s - \phi_l$ is the electric potential drop across the bulk electrolyte and the reaction plan, and (2) a modified Langmuir isotherm ("Model - Modified Langmuir"), i.e., $K_{\mathrm{eq}} = \exp\left(-\frac{\Delta G^0_{\mathrm{ad}}}{R_g T}\right) \exp\left(-\frac{z_{\mathrm{SnII}} F \Delta\phi_{\mathrm{eff}}}{R_g T}\right)$, where $\Delta\phi_{\mathrm{eff}} = c^{\xi}_{\mathrm{SnII}} \Delta\phi$ is the empirically-derived effective electric potential drop across the bulk electrolyte and the reaction plan, and ξ is a empirical parameter. We use $c_{sf,\mathrm{SnII}}$ to replace c_{SnII} in the Butler-Volmer equation (Equation (15)) to consider the deviation of surface concentration from the bulk electrolyte, as well as its impact on the electrochemical reactions.

As shown in Figure 8a, the model incorporating the standard Langmuir isotherm does not notably modify the 2nd-stage discharge curve. Due to the relatively large $\Delta\phi$ at the beginning of the 2nd-stage discharge, $K_{\mathrm{eq}} \gg 1$ and $c_{sf,\mathrm{SnII}} \approx c^{\mathrm{m}}_{sf,\mathrm{SnII}}$. The reaction rate and cell voltage remain almost constant until the c_i approaches 0 and $c_{s,\mathrm{SnII}} \propto c_{\mathrm{SnII}}$. In contrast, the model using a modified Langmuir isotherm ($c^{\mathrm{m}}_{sf,\mathrm{SnII}} = 0.01\,\mathrm{mol/m^2}$ and $\xi = 0.65$) outperforms the prior model and presents a much better match with the 2nd-stage discharge (Figure 8a). In this model, K_{eq} and $c_{sf,\mathrm{SnII}}$ decrease nonlinearly with c_{SnII}. To maintain a constant current, the anode electropotential needs to increase (i.e., the cell voltage will decrease). Accordingly, the RMSE decreases from 0.15 V to 0.068 V. Furthermore, the new model is validated by simulating the charge–discharge curves at three other rates. All simulated curves align well

with the experimental data (Figure 9). The RMSEs are 0.026 V∼0.057 V for charge, and 0.069 V∼0.11 V for discharge. These observations reveal additional interfacial interactions between $Sn(OH)_3^-$ and carbon surfaces.

We also perform a global sensitivity analysis on the same uncertain reaction parameters for those in Section 3.1.3 with additional parameters for nucleation (i.e., the product of nucleation probability and frequency, $Z \cdot f$) and adsorption (i.e., the empirical parameter ξ) (Figure S9). The results suggest that $A_{0,an}$, $i_{0,1}$, and $i_{0,2}$ collectively control the voltage plateau—their first- and second-order Sobol's indices add up to 0.84 for charge and 0.48 for discharge. These observations show the dominant role of the reactive surface area and exchange current densities for the anode reactions.

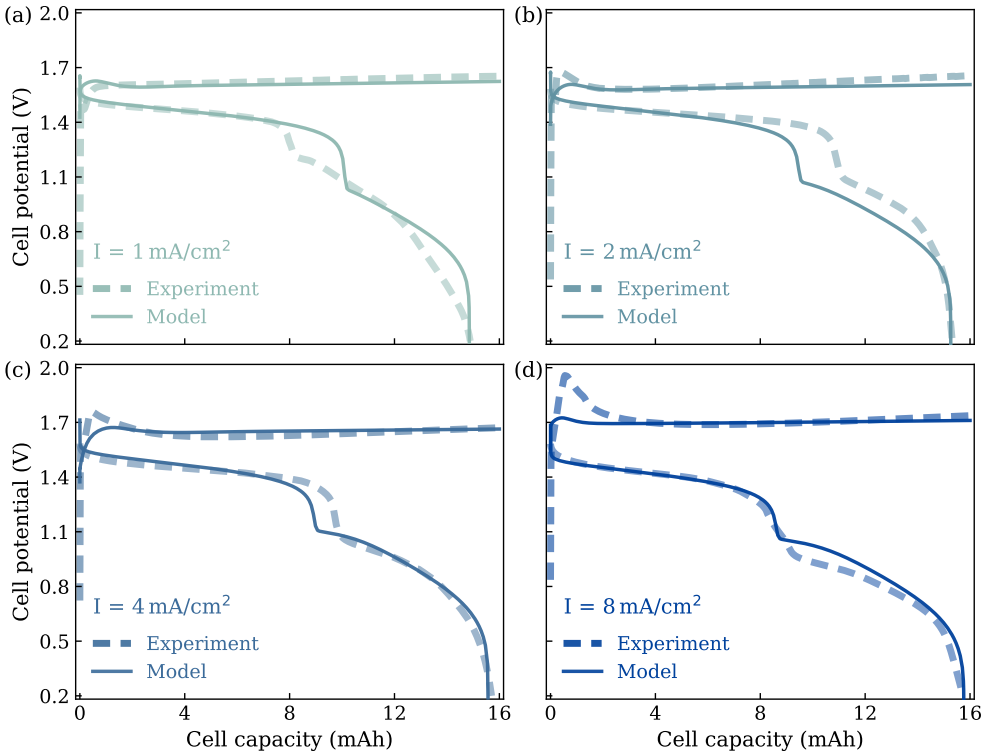

Figure 9: Modeled vs. measured galvanostatic charge–discharge curves of an alkaline Sn–NiOOH battery cell using a carbon-based anode and an anion exchange membrane as the separator. The cell is charged and discharged at four current densities (i.e., $i_{tot}(t) = 1$, 2, 4, and 8 mA/cm^2).

4 Discussion

We examine the modeling results to elucidate the mechanisms that control aqueous battery performance (Section 4.1) and inform the optimization of cell architecture and cycling protocols (Section 4.2). We also comment on potential model extensions for capturing more involved physics and electrochemistries in aqueous batteries (Section 4.3).

4.1 Mechanistic understandings of physical and electrochemical processes

4.1.1 Acidic H_2–Mn battery

Our model indicates that the performance of the acidic H_2–Mn battery is primarily limited by reactant transport during charge. During charge, due to the higher overpotential at locations close to the anode–current collector interface (at smaller spatial coordinate x), H_2 evolution and H^+ consumption reactions are faster and consume more H^+. In the meantime, the H^+ supply is limited by diffusion, with both molecular diffusion and Grotthuss-type structural diffusion captured in the model by an effective H^+ diffusion coefficient (Table S5). They collectively lead to a substantial pH rise, especially at the locations close to the anode–current collector interface (Figure 3b). In contrast, Mn^{2+} concentration remains relatively uniform across both space and time, except near the cathode terminal (at large spatial coordinate x), where a pronounced gradient develops. These findings suggest that under high charge capacity conditions, reactant depletion may become more severe; specifically, H^+ at the anode and Mn^{2+} at the cathode due to limited transport at the extremes of the cell. Therefore, a lower charge rate or a thinner electrode could enable achieving higher utilization of active materials. Our model can be used to identify transport-limited regimes and guide the selection of charge–discharge rates or electrode thickness that mitigate these limitations.

4.1.2 Near-neutral Zn–MnO_2 battery

For near-neutral Zn–MnO_2 aqueous batteries, one main challenge is to resolve the discharge reaction mechanisms at the MnO_2 cathode. As discussed in Section 3.1.2, this remains an open question. To help address this ambiguity, our model conceptualizes both H^+ (de)intercalation and ZHS formation but treats these two reactions separately, which enables us to examine their influence on pH evolution and the subsequent impact on the 2^{nd}-stage discharge. Our model outperforms two recently reported models[18,19] in simulating experimentally measured charge–discharge curves. More importantly, our simulations suggest that competition between reversible H^+ (de)intercalation and ZHS deposition/dissolution can account for the characteristic voltage rebound at the onset of the second discharge plateau, which is oftentimes not well captured in the other simulated discharge plateaus. We demonstrate that while the first discharge plateau is dominated by Zn^{2+} intercalation, the second plateau corresponds to H^+ intercalation and ZHS formation (Figures 4b–c and 5). We observe that ZHS formation occurs predominantly during the second discharge plateau (Figure 4c). These findings suggest that the interplay between these reactions is crucial in determining reversibility and cycling stability. This is consistent with recent experimental observations and theoretical analysis[19,21,22].

Finally, we explore other proposed discharge reaction mechanisms by three additional simulations: (1) Zn^{2+} intercalation and H^+ intercalation, but without ZHS formation; (2) Zn^{2+} intercalation only; (3) H^+ intercalation only. As shown in Figure S10, each of these alternate reaction mechanisms fails to capture the key features of the experimental discharge reaction. The model not considering ZHS formation will significantly underestimate the 2^{nd}-stage discharge voltage, while the models considering a single intercalation reaction (either Zn^{2+} or H^+) cannot replicate the two-stage discharge behavior. The simulated concentrations of intercalated Zn^{2+} and H^+, pH, and surface area of ZHS in each case are shown in Figure S11. This analysis further supports our model representation of the reaction mechanisms, which includes Zn^{2+} (de)intercalation, H^+ (de)intercalation, ZHS precipitation/dissolution,

and the interactions between them.

4.1.3 Alkaline Sn-anode battery

The behaviors of alkaline Sn–NiOOH batteries have been effectively captured by our model despite the complexity introduced by the asymmetric four-electron charge/discharge reactions and the sensitivity to substrate-dependent kinetics. The simulations show strong agreement with experimental data on both copper and carbon anode substrates, though in order to accurately reproduce the distinct charge–discharge behavior of carbon-based anode substrates, the model incorporates metal nucleation and surface adsorption phenomena. Under the tested cycling conditions (Figures 6 and 9), ion transport does not limit performance, as only a small fraction of the theoretical capacity is accessed (Figure S5).

Higher utilization of the active materials needs to be achieved to lower the cost of aqueous batteries, but can introduce new phenomena that must be captured by the model. At high plated capacities of alkaline Sn–NiOOH batteries, carbon substrates often demonstrate inhomogeneous nucleation and plating, while copper substrates experience chemical reactivity with the plated Sn, resulting in intermetallic alloying and strain-induced inhomogeneous plating[5]. Both of these phenomena result in spatially heterogeneous growth of the solid Sn surfaces and lead to significant spatial variations in $Sn(OH)_6^{2-}$ concentration. When approaching a higher utilization, sluggish $Sn(OH)_6^{2-}$ transport from low to high reaction rate areas could cause depletion of $Sn(OH)_6^{2-}$. If the transport time scale is longer than the reaction time scale, the reaction will be limited by $Sn(OH)_6^{2-}$ transport. The transport limitation can potentially lead to a rapid increase in cell potential and trigger HER to dominate. In the following section, we will demonstrate the application of our model for studying the impact of the transport limitation on the cell potential and its impact on the occurrence of HER.

4.2 Model application towards higher-utilization aqueous batteries

We examine the impact of charging rates on the occurrence of HER and the corresponding utilization in alkaline Sn–NiOOH batteries. We apply the model described in Section 3.2 that accounts for nucleation to predict the onset of HER by simulating the charge curves of the alkaline Sn–NiOOH battery at four different rates: $i_{\mathrm{tot}}(\mathrm{t}) = 1$, 4, 8, and 16 $\mathrm{mA/cm^2}$ (Figure 10). For all simulations, we use a cell potential threshold (2 V) determined from high-utilization experimental data to identify the utilization at which HER becomes dominant. The simulation results suggest a notable transport limitation at the higher rates (Figure 10a–b), which leads to a rapid increase in the cell potential corresponding to the depletion of the main reactant ($\mathrm{Sn(OH)_6^{2-}}$). Consequently, HER occurs at a lower utilization (approximately 77.9%) and reduces the usage of all $\mathrm{Sn(OH)_6^{2-}}$ in the system at higher rates.

Transport limitations are potentially more significant in experiments where the anode substrate (i.e., carbon felt) has a three-dimensional structure with heterogeneous surface properties. Additionally, the system can be further complicated in configurations where the anode length and width (dimensions in the y and z directions) are much larger than the thickness (dimension in the x direction). Therefore, the transport pathways for $\mathrm{Sn(OH)_6^{2-}}$ in a three-dimensional system may exceed the thickness, leading to a longer transport time scale and more significant transport limitations. To achieve higher utilization without significant HER, lower charge rates, in particular later in the charging process, are necessary. Our model can be used to estimate the optimal charge rate and guide the real-time control of the charge rate.

4.3 Model limitations

We note that a few assumptions and simplifications are employed in the current modeling framework. First, the model adopts a one-dimensional homogeneous representation, which

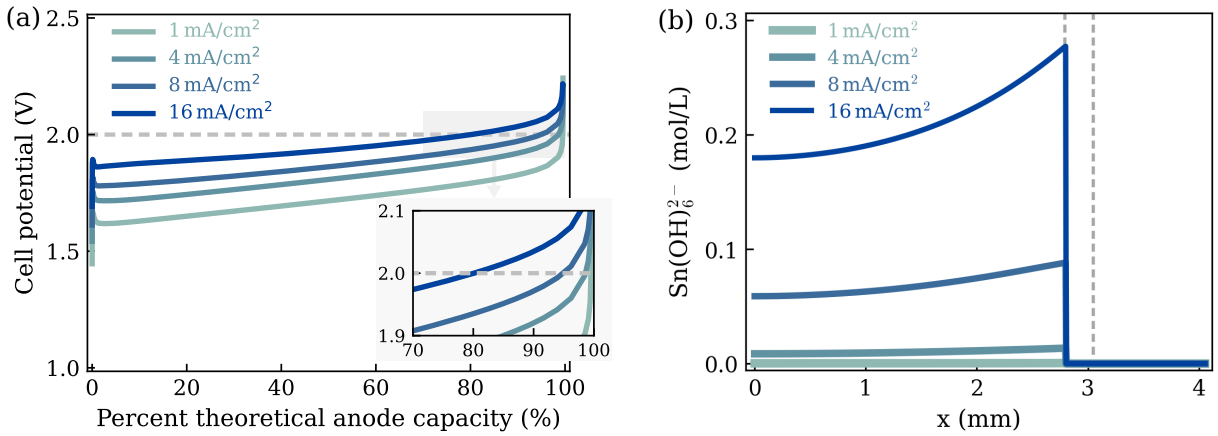

Figure 10: (a) Predictions on the onset of H_2 gas generation and utilization limit. The cell is charged and discharged at four current densities (i.e., $i_{tot}(t) = 1$, 4, 8, and 16 mA/cm^2). (b) The concentration profiles of $Sn(OH)_6^{2-}$ across the cell when the cell potential reaches 2 V.

does not account for three-dimensional structures and heterogeneity (e.g., surface chemistry). The importance of these factors can be further examined by extending our one-dimensional model formulations to a three-dimensional domain. Second, we did not account for ion diffusion inside the solid active materials during the intercalation and deintercalation processes because most experimental data (e.g., alkaline Sn–NiOOH batteries) were collected at a low utilization of the cathode active materials and the intra-particle diffusion process was not the limiting factor. For conditions where the utilization of cathode active materials is higher, the model can be extended to incorporate intra-particle diffusion processes by either using a simplified representation (e.g., spherical particles[19]) or an explicit three-dimensional representation of the active materials. Third, the model assumes dilute ion concentrations such that ion activities are equal to ion concentrations. In concentrated solutions, ion activities may be notably smaller than ion concentrations, meaning that the activity coefficient may change with the stage of charge as ions are generated or consumed. Under those conditions, advanced theories (e.g., extended Debye–Hückel theory, Specific Interaction Theory, Pitzer equation, or molecule-level theory) may be necessary to compute the actual activities for the transport and reaction models. For these advanced models, more experimental efforts are desired to determine the unknown parameters, and once experimental data and model

parameterization are available, they can be incorporated into the model. Finally, we note that the model does not yet account for material degradation mechanisms and is therefore not readily applicable to long-term cycling or calendar-aging prediction. However, as demonstrated in Section 3.2, our model provides the flexibility to incorporate the above additional physical processes to investigate any aqueous battery system of interest.

5 Conclusions

We present a versatile modeling framework for simulating aqueous battery charge–discharge performance. The framework captures multispecies ion transport, charge transport, and reactions in the liquid electrolyte; the reactions and charge exchange at the interfaces between the liquid electrolyte and the solid substrate; solid-phase charge transport; as well as temporal and spatial variations in pH and reactive surface areas. We solve the nonlinear model under arbitrary initial and boundary conditions using a backward-Euler finite-volume method, which provide accurate predictions on the potentiostatic or galvanostatic charge–discharge curves of aqueous batteries under a wide range of chemistries and cycling conditions. Comprehensive model-data comparisons demonstrate the model's capability of capturing the complex physical and electrochemical processes during charge and discharge of a wide range of aqueous batteries. Furthermore, the model can be extended to simulate more involved physical processes such as metal nucleation and interfacial adsorption processes.

The model offers a computationally efficient tool to test hypotheses and guide architectural design for aqueous batteries. For systems where the physical mechanisms are poorly characterized, the model can be applied to test hypotheses for the underlying mechanisms (e.g., reaction pathways) derived from experimental observations and first-principle theories (e.g., density functional theory and molecular dynamics). This iterative process is anticipated to advance the characterization of key controlling physical, chemical, and electrochemical processes on the performance of aqueous batteries. For aqueous batteries where

the physical mechanisms are well-characterized, the model can be directly applied to simulate their charge–discharge curves and inform ideal materials properties and tailored cycling protocols for optimal performance. Combining our modeling efforts with rigorous experimental validations, we aim to advance the development of higher energy density, longer cycle life, and lower cost of aqueous batteries for grid-scale energy storage.

Acknowledgement

This work is related to the Aqueous Battery Consortium, an energy innovation hub under the US Department of Energy, Office of Basic Energy Sciences, Division of Materials Science and Engineering. The authors thank Diego Rivera, Alexis Geslin, Katherine Harmon, and Willow Thompson for their insightful review comments. Additionally, we appreciate the valuable discussions on battery modeling with Shaunak Joshi, Nik Leuenberger, and Daniel Tartakovsky.

Supporting Information Available

Supporting Information (SI) provides experimental information and supplementary figures.

References

(1) Fang, G.; Zhou, J.; Pan, A.; Liang, S. Recent advances in aqueous zinc-ion batteries. *ACS Energy Letters* **2018**, *3*, 2480–2501.

(2) Zhu, Z.; Jiang, T.; Ali, M.; Meng, Y.; Jin, Y.; Cui, Y.; Chen, W. Rechargeable batteries for grid scale energy storage. *Chemical Reviews* **2022**, *122*, 16610–16751.

(3) Zhou, W.; Song, M.; Liang, P.; Li, X.; Liu, X.; Li, H.; Zhang, T.; Wang, B.; Zhao, R.;

Zhao, Z.; others High-energy Sn–Ni and Sn–Air aqueous batteries via stannite-ion electrochemistry. *Journal of the American Chemical Society* **2023**, *145*, 10880–10889.

(4) Wang, J.; Catalina, S. K.; Jiang, Z.; Xu, X.; Zhou, Q. T.; Chueh, W. C.; Mefford, J. T. A reversible four-electron Sn metal aqueous battery. *Joule* **2024**, *8*, 3386–3396.

(5) Wang, J.; Catalina, S. K.; Xu, X.; Jiang, Z.; Zhou, T. Q.; Chueh, W. C.; Mefford, J. T. Cu substrate as bi-directional kinetic promoter in four-electron Sn aqueous batteries. Manuscript in preparation.

(6) Lee, D.-C.; Lei, D.; Yushin, G. Morphology and Phase Changes in Iron Anodes Affecting their Capacity and Stability in Rechargeable Alkaline Batteries. *ACS Energy Letters* **2018**,

(7) D'Ambrose, M. J.; Turney, D. E.; Yadav, G. G.; Nyce, M.; Banerjee, S. Material Failure Mechanisms of Alkaline Zn Rechargeable Conversion Electrodes. *Applied Energy Materials* **2021**,

(8) Sui, Y.; Ji, X. Anticatalytic strategies to suppress water electrolysis in aqueous batteries. *Chemical Reviews* **2021**, *121*, 6654–6695.

(9) He, Y.; Shang, W.; Ni, M.; Huang, Y.; Zhao, H.; Tan, P. In-situ observation of the gas evolution process on the air electrode of Zn-air batteries during charging. *Chemical Engineering Journal* **2022**, *427*, 130862.

(10) Chao, D.; Zhou, W.; Xie, F.; Ye, C.; Li, H.; Jaroniec, M.; Qiao, S.-Z. Roadmap for advanced aqueous batteries: From design of materials to applications. *Science advances* **2020**, *6*, eaba4098.

(11) Newman, J. S.; Tobias, C. W. Theoretical analysis of current distribution in porous electrodes. *Journal of The Electrochemical Society* **1962**, *109*, 1183.

(12) Plett, G. L. *Battery management systems, Volume I: Battery modeling*; Artech House, 2015.

(13) Brosa Planella, F.; Ai, W.; Boyce, A. M.; Ghosh, A.; Korotkin, I.; Sahu, S.; Sulzer, V.; Timms, R.; Tranter, T. G.; Zyskin, M.; others A continuum of physics-based lithium-ion battery models reviewed. *Progress in Energy* **2022**, *4*, 042003.

(14) Kumaresan, K.; Mikhaylik, Y.; White, R. E. A Mathematical Model for a Lithium–Sulfur cell. *Journal of the Electrochemical Society* **2008**, *155*, A576.

(15) Ren, Y.; Zhao, T.; Liu, M.; Tan, P.; Zeng, Y. Modeling of Lithium-Sulfur Batteries Incorporating the Effect of Li_2S Precipitation. *Journal of Power Sources* **2016**, *336*, 115–125.

(16) Parke, C. D.; Teo, L.; Schwartz, D. T.; Subramanian, V. R. Progress on continuum modeling of lithium–sulfur batteries. *Sustainable Energy & Fuels* **2021**, *5*, 5946–5966.

(17) Clark, S.; Latz, A.; Horstmann, B. Rational development of neutral aqueous electrolytes for zinc–air batteries. *ChemSusChem* **2017**, *10*, 4735–4747.

(18) Bernard, J. C.; Wang, Z.; Yan, S.; Takeuchi, E. S.; Marschilok, A. C.; Takeuchi, K. J.; West, A. C. Physics-Based Continuum Modeling for an Aqueous Rechargeable Zn/MnO2 Battery. *Journal of The Electrochemical Society* **2024**, *171*, 050502.

(19) Herrmann, N. J.; Euchner, H.; Groß, A.; Horstmann, B. The Cycling Mechanism of Manganese-Oxide Cathodes in Zinc Batteries: A Theory-Based Approach. *Advanced Energy Materials* **2024**, *14*, 2302553.

(20) Chen, W.; Li, G.; Pei, A.; Li, Y.; Liao, L.; Wang, H.; Wan, J.; Liang, Z.; Chen, G.; Zhang, H.; Wang, J.; Cui, Y. A manganese–hydrogen battery with potential for grid-scale energy storage. *Nature Energy* **2018**, *3*, 428–435.

(21) Wu, D.; King, S. T.; Sadique, N.; Ma, L.; Ehrlich, S. N.; Ghose, S.; Bai, J.; Zhong, H.; Yan, S.; Bock, D. C.; others Operando investigation of aqueous zinc manganese oxide batteries: multi-stage reaction mechanism revealed. *Journal of Materials Chemistry A* **2023**, *11*, 16279–16292.

(22) Lim, W.-G.; Li, X.; Reed, D. Understanding the role of zinc hydroxide sulfate and its analogues in mildly acidic aqueous zinc batteries: a review. *Small Methods* **2024**, *8*, 2300965.

(23) Pourbaix, M. Atlas of electrochemical equilibria in aqueous solutions. *NACE* **1966**,

(24) Pan, H.; Shao, Y.; Yan, P.; Cheng, Y.; Han, K. S.; Nie, Z.; Wang, C.; Yang, J.; Li, X.; Bhattacharya, P.; others Reversible aqueous zinc/manganese oxide energy storage from conversion reactions. *Nature Energy* **2016**, *1*, 1–7.

(25) Bernard, J. C.; Hill, R. C.; Wang, Z.; Takeuchi, E. S.; Marschilok, A. C.; Yan, S.; Takeuchi, K. J.; West, A. C. Electrolyte Engineering in Aqueous Zn/MnO2 Batteries: Effects of pH and ZnSO4 on Electrochemical Behavior and Degradation Mechanisms. *Journal of The Electrochemical Society* **2025**, *172*, 100509.

(26) Alfaruqi, M. H.; Gim, J.; Kim, S.; Song, J.; Jo, J.; Kim, S.; Mathew, V.; Kim, J. Enhanced reversible divalent zinc storage in a structurally stable α-MnO2 nanorod electrode. *Journal of Power Sources* **2015a**, *288*, 320–327.

(27) Lv, H.; Song, Y.; Qin, Z.; Zhang, M.; Yang, D.; Pan, Q.; Wang, Z.; Mu, X.; Meng, J.; Sun, X.; others Disproportionation enabling reversible MnO2/Mn2+ transformation in a mild aqueous Zn-MnO2 hybrid battery. *Chemical Engineering Journal* **2022**, *430*, 133064.

(28) Juran, T. R.; Young, J.; Smeu, M. Density functional theory modeling of MnO2 polymorphs as cathodes for multivalent ion batteries. *The Journal of Physical Chemistry C* **2018**, *122*, 8788–8795.

(29) Elsner, A.; Wagner, A.; Aste, T.; Hermann, H.; Stoyan, D. Specific surface area and volume fraction of the cherry-pit model with packed pits. *The Journal of Physical Chemistry B* **2009**, *113*, 7780–7784.

(30) Chiu, S. N.; Stoyan, D.; Kendall, W. S.; Mecke, J. *Stochastic geometry and its applications*; John Wiley & Sons, 2013.

(31) Zhou, Y.; Wang, X.; Shen, X.; Shi, Y.; Zhu, C.; Zeng, S.; Xu, H.; Cao, P.; Wang, Y.; Di, J.; Li, Q. 3D confined zinc plating/stripping with high discharge depth and excellent high-rate reversibility. *Journal of Materials Chemistry A* **2020**, *8*, 11719–11727.

(32) Sobol, I. M. Global sensitivity indices for nonlinear mathematical models and their Monte Carlo estimates. *Mathematics and computers in simulation* **2001**, *55*, 271–280.

(33) Saltelli, A.; Ratto, M.; Andres, T.; Campolongo, F.; Cariboni, J.; Gatelli, D.; Saisana, M.; Tarantola, S. *Global Sensitivity Analysis: The Primer*; Wiley, 2008.

(34) Wang, J. Developing a Four-electron Sn Anode for Aqueous Batteries. Ph.D. Thesis, Stanford University, 2024.

(35) Schmickler, W.; Santos, E. *Interfacial electrochemistry*; Springer Science & Business Media, 2010.